Research Square

Preprints are preliminary reports that have not undergone peer review.
They should not be considered conclusive, used to inform clinical practice,
or referenced by the media as validated information.

Machine Learning-based Surrogate Model for Melt Pool Control in Laser-based Direct Energy Deposition

Runeal Ramma

runeal.ramma@upc.edu

RMIT University

Carlos Moreira

International Center for Numerical Methods in Engineering

Michele Chiumenti

Universitat Politècnica de Catalunya

Manuel Alejandro Caicedo

Universitat Politècnica de Catalunya

Raj Das

RMIT University

Zhijun Ji

Bejing Institute of Aeronautical Materials

Andrey Molotnikov

RMIT University

Research Article

Keywords: Additive manufacturing, laser-based direct energy deposition, processing parameters optimization, machine learning, surrogate controller, run-time control.

Posted Date: July 27th, 2026

DOI: https://doi.org/10.21203/rs.3.rs-8641262/v3

License: This work is licensed under a Creative Commons Attribution 4.0 International License.
Read Full License

Additional Declarations: The authors declare no competing interests.

Machine Learning-based Surrogate Model for Melt Pool Control in Laser-based Direct Energy Deposition

Runeal Ramma[*,1,2,3], Carlos A. Moreira[2], Michele Chiumenti[2,3], Manuel A. Caicedo[4], Raj Das[1], Zhijun Ji[5], Andrey Molotnikov[1]

[1] Centre for Additive Manufacturing, School of Engineering, RMIT University, 124 La Trobe Street, Melbourne, Australia
[2] International Center for Numerical Methods in Engineering (CIMNE), Edificio C1, Campus Norte, Gran Capitán s/n, 08034 Barcelona, Spain
[3] Technical University of Catalonia, Edificio C1, Campus Norte, Gran Capitán s/n, 08034 Barcelona, Spain
[4] Technical University of Catalonia, Barcelona East School of Engineering (EEBE), Av. Eduard Maristany 16, 08019 Barcelona, Spain
[5] 5 AECC Beijing Institute of Aeronautical Materials, Beijing 100095, China

Corresponding author: s3625767@student.rmit.edu.au or runeal.ramma@upc.edu

Abstract

Laser-based Direct Energy Deposition (DED-LB) is a key technology in both manufacturing and repair of components within metal Additive Manufacturing (AM). However, challenges such as heat accumulation and insufficient dynamic process control restrict its broader adoption. This work proposes a novel strategy to stabilize the deposition process by integrating a Machine Learning (ML) model as a ML-based surrogate controller, coupled with a Finite Element (FE) solver for run-time process control. The FE framework performs thermal analysis of the DED-LB process and generates High-Fidelity (HF) synthetic data through an offline optimization approach for training the ML model. The architecture of the ML model is optimized via hyperparameter tuning and validated on an independent case outside the training dataset. The resulting ML-based surrogate controller, coupled with the FE solver, analyzes melt pool morphology and thermal profiles in run-time and outputs corrective laser power adjustments to maintain a constant melt pool penetration depth. This closed-loop system enables autonomous control and rapid dynamic response, ensuring consistent thermal management throughout the deposition process. Three scanning-sequence scenarios are presented to evaluate the performance of the run-time control system. The results indicate that integrating this framework maintains a stable melt pool penetration depth, thereby enhancing geometric precision and reliability in DED-LB through tailored time-series power profiles, while reducing the computation time to one-third relative to the offline iterative optimization approach. Among the three sequences, two were not included in the training dataset of the ML model, and the accurate control of these cases demonstrates the robust generalization capability of the ML-based surrogate controller and confirms its suitability for precise and scalable control of metal AM processes.

Keywords: Additive manufacturing, laser-based direct energy deposition, processing parameters optimization, machine learning, surrogate controller, run-time control.

1 Introduction

Laser-based Direct Energy Deposition (DED-LB) is an Additive Manufacturing (AM) process that uses focused thermal energy in the form of a laser to fuse molten material in a layer-by-layer manner to manufacture a part. This method involves feeding metal powder or wire into a laser-generated melt pool on a substrate, facilitating precise control over material addition and enabling the fabrication of complex geometries or the repair of existing components. This advanced technique is especially appealing to the aerospace and automotive industries for component repair, lightweight structural designs, and rapid prototyping. However, DED-LB faces challenges with effective heat management during the deposition process. Employing constant process parameters, such as a constant laser power supply leads to significant heat accumulation in the deposition chamber, which causes thermal distortion, elevated residual stresses, and substrate cracking [1]. One of the primary concerns in DED-LB is the accuracy of the thermal input into the melt pool, as proper heat input is crucial for controlling its size and shape. Additionally, effective heat management requires controlling the thermal profile to prevent both overheating and excessive cooling of the substrate, which can lead to geometric distortion of the deposited layers [2].

As outlined in [3], controllers can be employed during the deposition process to assess the melt pool, thereby enabling process-parameter adjustment based on experimental or numerical feedback. The control and optimization of processing parameters are often more effectively achieved using numerical approaches, which are less expensive than experimental trials and offer greater flexibility and efficiency in identifying optimal parameter combinations. One approach is to employ a simulation-guided process planning to identify suitable parameter combinations prior to the printing process. The work conducted by [4] used a closed loop approach with a proportional-integral controller connected to numerical simulations to stabilize the melt pool temperature by adjusting the laser power based on run-time feedback data from the simulations. In that sense, [5] used three different controllers to assess their performance and determine their suitability throughout the different stages of the deposition process. Controllers can also be utilized in an optimization loop, where processing parameters are refined prior to the actual printing process. For example, the study by [6] used both simulation and experimental methods to vary the scanning sequence and interlayer cooling time, identifying optimal parameters to minimize residual stresses in titanium alloy AM parts. However, once tuned, parameter-dependent controllers may not adapt well to changes in the process or operating environment without further re-tuning [7].

On the other hand, surrogate models have been used to accelerate the optimization of processing parameters in DED-LB, providing efficient approximations to High-Fidelity (HF) simulations or experiments while enabling systematic explorations of the design space. In the work conducted by [8], Multi-Fidelity (MF) Gaussian Process Regression (GPR) surrogate models have been used in DED-LB to combine HF Finite Element (FE) and Low-Fidelity (LF) analytical models for temporally resolved forward and inverse process mapping with Bayesian optimization under computational constraints. This is in line with the work conducted by [9], where a GPR model has been used as a surrogate model in DED-LB to map processing parameters to single-track geometries with explicit uncertainty quantification, enabling an inverse, user-guided workflow that proposes parameter sets likely to achieve a target track shape and thereby reducing reliance on trial-and-error tuning. Similarly, [10] developed a combined physical-simulation and Machine Learning (ML) framework in which a powder-scale high-precision model generates a small but accurate dataset used to train a GPR surrogate of track geometry and dilution, and particle swarm optimization is then applied to this surrogate to obtain experimentally validated optimal process schemes. Despite these advances, many surrogate models, particularly simple response surface-based approaches, struggle to represent the strong nonlinear couplings inherent in DED-LB. In this context, ML models can learn underlying patterns and better accommodate unforeseen disturbances [11], making them more robust and suitable for determining optimal processing parameters for the inherently dynamic DED-LB process.

ML has proven to be a valuable asset in the field of AM and by utilizing its advanced capabilities, various aspects of the process can be revolutionized [12]. The application of ML in AM has been employed in areas such as defect detection, material property prediction, and the optimization of processing parameters [13, 14]. The research conducted by [15] illustrates the diverse techniques applicable to ML within the realm of AM. The study suggests that for the optimization and prediction capabilities of the DED-LB deposition process, a supervised or semi-supervised Regression-Artificial Neural Network (R-ANN) would be the most suitable selection. In reference [16], an R-ANN was developed through supervised learning to predict the melt pool morphology offline, based on the printing parameters or the evolution of the

thermal field [17]. Simulated data is preferred as it is relatively easier and cheaper to generate synthetic data, i.e., based on a Finite Element Method (FEM) of the process as compared to experimental data. Therefore, ML models trained on HF databases can be used to reveal hidden dependencies of features through virtual experiments, offering a valuable tool for improving material properties [18]. Multiple trials were conducted to control the melt pool size using different techniques such as a Q-learning algorithm [19] and Proximal Policy Optimization (PPO) [20] based on reinforcement learning, classification of melt pool images using deep convolutional neural networks [21–23]. Substantial effort has been directed toward accelerating the determination of optimal processing parameters for the DED-LB process. Nevertheless, there remains a gap for frameworks that both compute these parameters efficiently and can adapt to new scanning sequences while rapidly providing an accurate preliminary processing-parameter window to ensure the required geometric accuracy and repeatability during printing.

The proposed method aims at controlling the heat accumulation within the deposition chamber by modulating the power supply of the laser through a fast ML-based surrogate controller. This approach is executed through two distinct steps via numerical techniques. The first one involves an iterative a-posteriori loop designed to adjust the power supply to maintain a user-defined parameter constant, in this case, the penetration depth of the laser along the deposition process. This will generate precise data that accurately represents the deposition process, favoring HF simulations over experimental approaches for their ease and cost-effectiveness. The second strategy leverages the iterative optimization method to develop an a-priori approach based on an Artificial Intelligence (AI). The latter is trained from simulated offline data and operates within a computational environment to continuously regulate and maintain a constant penetration depth during the printing process. A correlation analysis has been used to assess the strength of the relationship between features in the generated synthetic dataset, assisting in identifying interdependencies among processing parameters as denoted by [24]. [25] demonstrated that selecting the most significant input parameters is an effective approach to improve the development of an accurate ML-driven regression model. Penetration depth of the laser has been explicitly identified as the control parameter to ensure reproducibility and consistent quality throughout the deposition process. This parameter is of meaningful interest due to its importance in determining the fusion boundary between the deposition layers, which will further influence defect types, such as keyhole porosity or lack of fusion [26], achieving the desired microstructure evolution and material properties [4], and determining the geometric accuracy of the fabricated part [27]. In [28], the authors systematically investigated the offline FE-based iterative optimization of the laser power profile for thin wall geometries. By tailoring the power profile to maintain a constant melt pool penetration depth, they demonstrated experimentally that dimensional accuracy can be substantially improved relative to a constant power input, which led to premature build termination. The use of a modulated power profile also promoted greater uniformity in the resulting microstructure than that observed in the incomplete constant-power build, underscoring the significant challenges associated with achieving consistent material properties over the entire build height. In that context, to enable the rapid identification of an optimized power profile of the DED-LB deposition process, this work couples a ML-based surrogate controller with a FE solver in a closed control loop. The framework delivers rapid corrective power predictions that continuously update the simulation during the run, achieving dynamic, scenario-specific control of melt pool penetration depth in a single iteration, even for scanning sequences not represented in the training dataset of the ML model.

The outline of the paper is as follows. In Section 2, the offline optimization strategy, featuring an iterative loop designed to adjust the power supply of the laser to maintain a constant melt pool depth, is presented. This forms the basis of generating training data for the ML model. Secondly, the development of the ML model is detailed, starting with identifying key input features through a correlation analysis and designing an optimized neural network using a Bayesian hyperparameter tuning approach. Subsequently, the R-ANN was validated and connected to a FE solver to create a closed-loop system that controls and maintains a consistent melt pool depth throughout the deposition process. Section 3 presents three numerical examples, a unidirectional thin wall, a hollow and an infill-partitioned cubic deposition, to showcase the performance of the run-time control system against the traditional offline approach to evaluate its accuracy. Section 4 presents concluding remarks on the efficacy of the proposed method, and future research lines are proposed.

2 Methodology

In DED-LB, the laser scanning sequence is governed by G-code, a key programming language for Computer Numerical Control (CNC) machining and 3D printing. In Layer Manufacturing Technology (LMT), components are sliced into layers in the xy-plane with the z-axis as the build direction. During numerical simulations, the G-code specifies tool paths and critical process parameters, including power supply, scanning speed, nozzle repositioning speed, dwell time, and layer thickness, which is controlled by the vertical movement of the printing head.

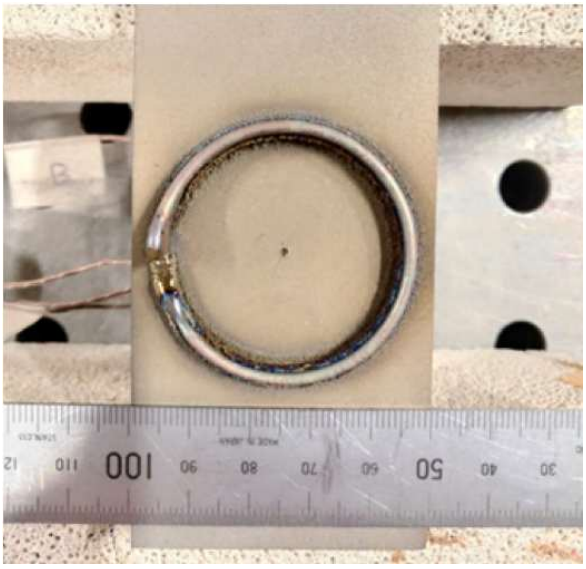
2.1 Numerical calibration

The simulations were conducted using *FEMUSS* (Finite Element Method Using Sub-grid Scales) [29–32], a multiphysics in-house software developed at the International Center for Numerical Methods in Engineering (CIMNE), which has the ability of High-Performance Computing (HPC) to solve the thermal analysis of the DED-LB deposition process and the qualification of the AM component. The thermal simulations were calibrated against experimental data by minimizing the error between measured and simulated thermal profiles. Temperature data from strategically placed experimental and virtual thermocouples are used to continuously update the heat transfer coefficients (HTCs) in the simulation, ensuring alignment with experimentally measured thermal profiles. This process employs *Dakota* [33], a robust optimization software developed by Sandia National Laboratories, coupled with *FEMUSS* and a Python script to ensure interoperability between them. The calibration print was performed on a TRUMPF TruLaser Cell 7020, a powder DED-LB machine, at the Centre for Additive Manufacturing, RMIT University. The calibration build consists of a thin cylinder with a diameter of 40 mm and a height of 10 mm (40 layers of 0.25 mm), deposited on a substrate measuring 100 mm × 50 mm × 12 mm. Both the deposit and the substrate are made from the titanium alloy Ti-6Al-4V and are supported by two refractory blocks, as shown in Figure1(a). Five thermocouples were employed, three embedded 5 mm below the surface along the centerline and two surface-welded to the underside of the substrate, as shown in Figure 1(b). All thermocouples were positioned on the underside to avoid direct exposure to the laser-beam radiation. The processing parameters consist of a laser power supply of 900 W, a scanning speed of 1200 mm/min, and a laser spot diameter of 1.75 mm. After completion of the build, the specimen is cooled to room temperature while the temperature evolution at all five thermocouples is continuously recorded. Thermocouple C was used to calibrate the HTC values because it is least affected by edge and transient effects and thus provides the most representative quasi-steady measurement of the thermal response. Model accuracy is quantified using the Root Mean Squared Error (RMSE) to assess the magnitude of the temperature prediction error and the coefficient of determination (R^2) to assess the degree of agreement between the simulated and experimental temperature histories, defined respectively as:

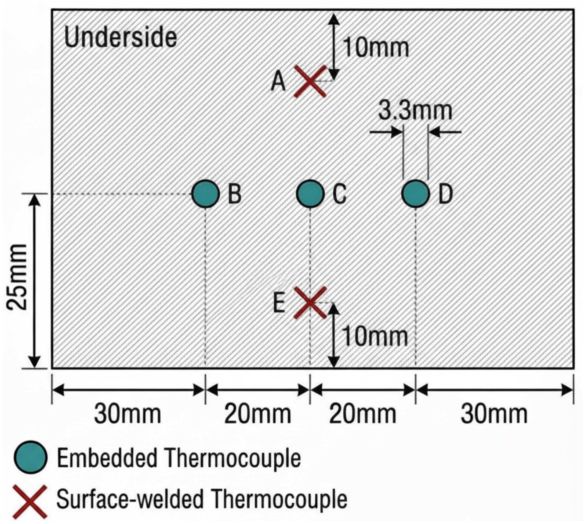
$$\mathrm{RMSE} = \sqrt{\frac{1}{N}\sum_{k=1}^{N}\left(T_k^{\mathrm{sim}} - T_k^{\mathrm{exp}}\right)^2} \tag{1}$$

$$R^2 = 1 - \frac{\sum_{k=1}^{N}\left(T_k^{\mathrm{sim}} - T_k^{\mathrm{exp}}\right)^2}{\sum_{k=1}^{N}\left(T_k^{\mathrm{exp}} - \overline{T}^{\mathrm{exp}}\right)^2} \tag{2}$$

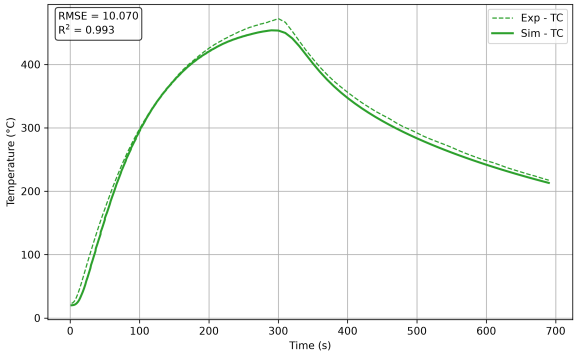
where, N denotes the number of data points, T_k^{sim} and T_k^{exp} are the simulated and experimental temperatures at time step k, respectively, and $\overline{T}^{\mathrm{exp}}$ is the mean of the experimental temperature history. A close agreement is observed between the recorded thermal history and the corresponding numerical results for the thermocouple at position C with a RMSE of 10.1°C and a R^2 of 0.993, as illustrated in Figure 1(c). To further validate model fidelity, the thermal fields at thermocouple position B are compared, showing close agreement with a RMSE of 10.5 °C and a R^2 of 0.99, as illustrated in Figure 1(d). These metrics demonstrate strong agreement between the calibrated model and the experimental measurements, corresponding to a calibrated power absorption coefficient of 0.3534 and four temperature-dependent HTC values, as summarized in Table 1.



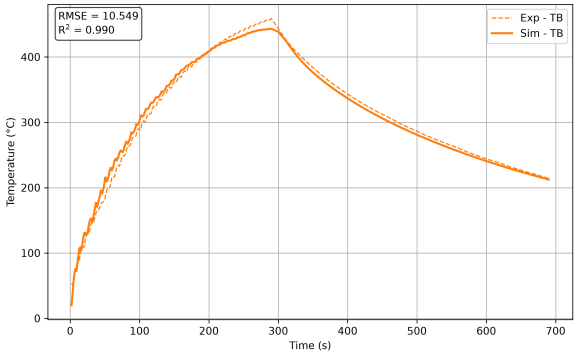
(a)



(b)



(c)



(d)

Figure 1: (a) Thin cylinder deposit for calibration, (b) substrate geometry and thermocouples position, (c) calibrated temperature evolution from thermocouple C, and (d) calibrated temperature evolution from thermocouple B. Reproduced with permission from [28].

Table 1: Calibrated HTC values for heat loss.

Temperature [°C]	HTC[W/m^2 °C]
20	4.211
600	27.33
1200	61.64
2500	134.23

2.2 A-posteriori offline optimization

The offline optimization method involves adjusting a processing parameter to meet a user-defined target value. In this case, the user defines a target melt pool penetration depth (D) (see Figure 2) and the power supply is iteratively adjusted within an optimization loop to achieve the desired penetration depth. The correction strategy is implemented by continuously adjusting the power supply based on the difference between the observed penetration depth (D_{obs}) and the target value (D_{target}) during the simulation of the

deposition process. To determine the target value of D, indicative of steady-state deposition, a simulation of a single track was performed, during which variations in penetration depth were monitored. A single track, 100 mm long and 3.5 mm wide, was simulated using a laser power of 2000 W and a scanning speed of 3000 mm/min. Upon achieving steady-state deposition, the associated representative penetration depth ($D_{target} = 0.40$ mm) was chosen as the governing criterion for the offline optimization process. This is in accordance with the work of [34] that suggests the remelting of the previous layer is primordial, as this will prevent delamination. Hence, $D = 0.40\,\text{mm}$ will melt approximately the equivalent of 2 layers, minimizing the risk of lack of fusion between adjacent layers.

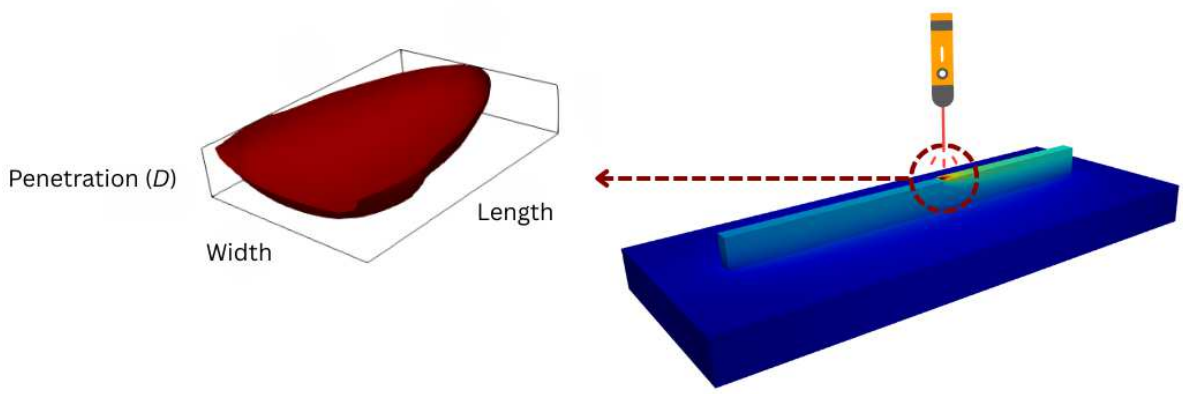


Figure 2: Schematic of the deposition process displaying the melt pool geometric characteristics.

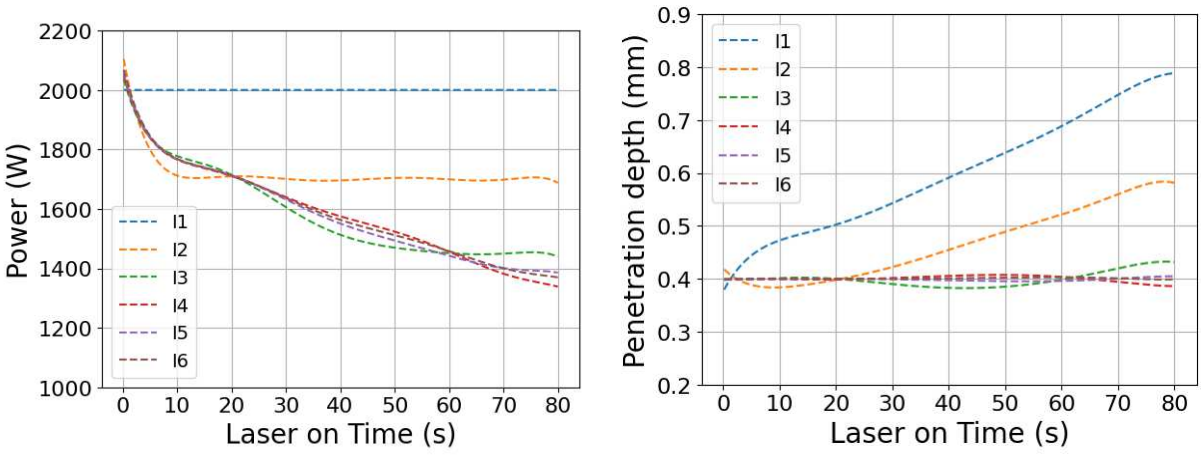
To achieve this, the error between the observed and target penetration depths is iteratively minimized by adjusting the current power ($P_{current}$). The corrected power, (P_{new}) is computed through a proportional feedback control approach, (K_p), illustrated as follows.

$$P_{new} = P_{current} \times K_p \tag{3}$$

The parameter K_p adjusts the magnitude and sensitivity of the power correction. To maintain system stability, it is imperative that K_p remains within defined limits, thereby mitigating the risk of instability. Consequently, K_p functions as a constrained correction factor, facilitating smoother adjustments and overall stability as follows.

$$K_{p_{\min}} < K_p = 1 + \frac{D_{\text{target}} - D_{\text{obs}}}{D_{\text{target}}} < K_{p_{\max}} \tag{4}$$

where K_{Pmin} and K_{Pmax} are user-defined lower and upper bounds. A comprehensive description of the a-posteriori optimization approach can be found in [28]. Figure 3 (a) and (b) illustrate an example for the convergence of the laser power supply and penetration depth during a thin wall deposition process. Notably, by the fifth iteration, the power stabilizes, yielding a nearly constant penetration depth of 0.40 mm. A sixth iteration was conducted to verify the convergence, thereby ensuring optimal power supply conditions.



(a) (b)

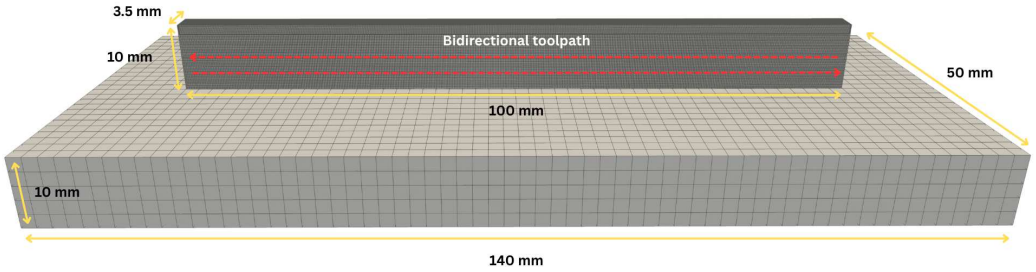
Figure 3: (a) Convergence study for the power profile of a thin wall deposition, (b) and the corresponding penetration curves.

2.2.1 Offline power control results

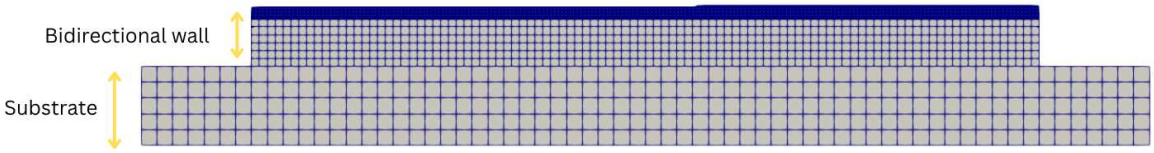
The geometry used to demonstrate the offline optimization approach consists of a bidirectional wall of height 10 mm (40 layers of 0.25 mm) and a length of 100 mm, illustrated in Figure 4(a). The material used for both the deposited component and the substrate is the titanium alloy Ti-6Al-4V [35] with a melting temperature of 1650 °C and high-productivity processing parameters were favored as detailed in Table 2. The mesh for the high-fidelity FE analysis is shown in Figure 4(b) and consists of 310,356 hexahedral 8-noded elements and 394,517 nodes. The simulation consists of 4205 time-steps with $\Delta t = 0.02$ s. A constant layer height ($h_0 = 0.25$ mm) is assumed in the simulations and the change of power is optimized with an attempt to keep the penetration depth of the laser constant. The designed power profile obtained through the offline optimization is illustrated in Figure 5(a), and was used to assess the difference in penetration depth when compared to a constant power supply. It can be observed in Figure 5(b–c) that by using a designed laser power profile, a relatively constant penetration depth of 0.40 mm was achieved whereas with the constant power supply, the penetration depth grows uncontrollably. Since the part is a thin wall, it is assumed that the melt pool width remains relatively uniform. Therefore, a cut section along the deposition path displaying the side view of the thin wall can be used to assess the evolution of the melt pool volume. Figure 6 illustrates the temperature contour plots when using a constant power supply and with the offline control. For the constant power supply, the melt pool volume increases rapidly during the progression of the deposition process, whereas the designed power profile results in a significantly more consistent melt pool volume. A controlled power supply maintains a relatively constant melt pool morphology, as observed from the top view of the controlled case, affirming a reduction in heat accumulation at the trailing area of the melt pool. This control improves the stability of the melt pool morphology, particularly the penetration depth, ultimately leading to a more geometrically accurate printed part as demonstrated in [28].

Table 2: Bidirectional wall process parameters.

Parameter	Value
Power [W]	2,000
Deposition speed [mm/min]	3,000
Repositioning speed [mm/min]	10,000
Laser spot diameter [mm]	3.5
Laser penetration depth [mm]	0.4
Layer height [mm]	0.25
Absorption efficiency [%]	35

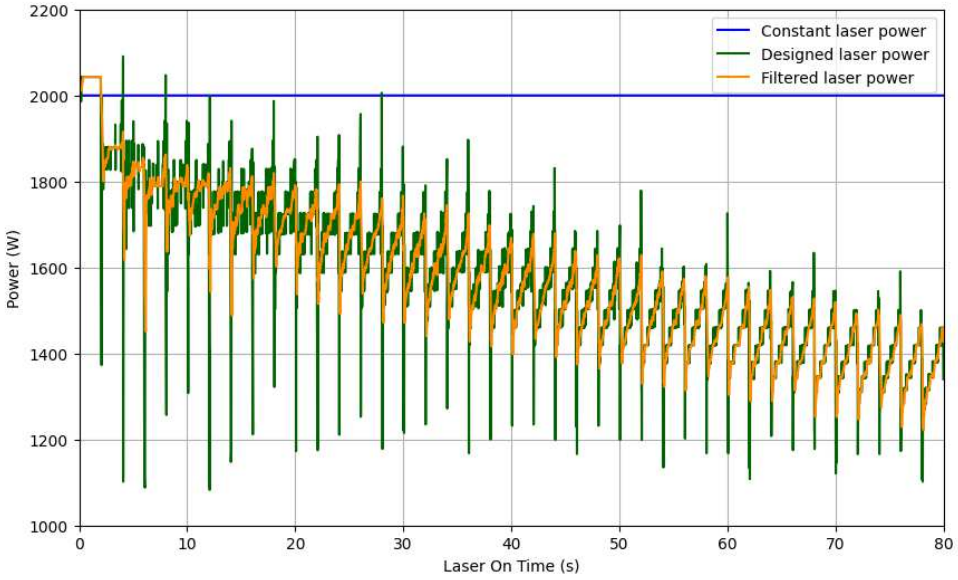


(a)

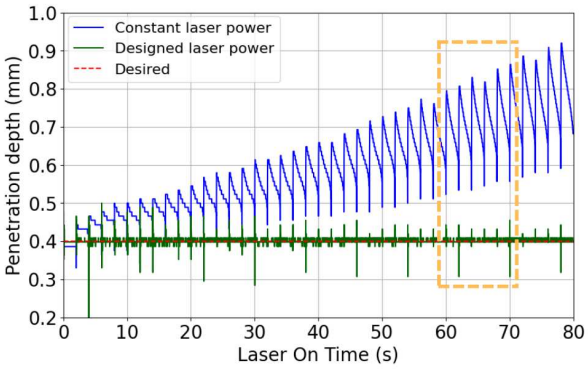


(b)

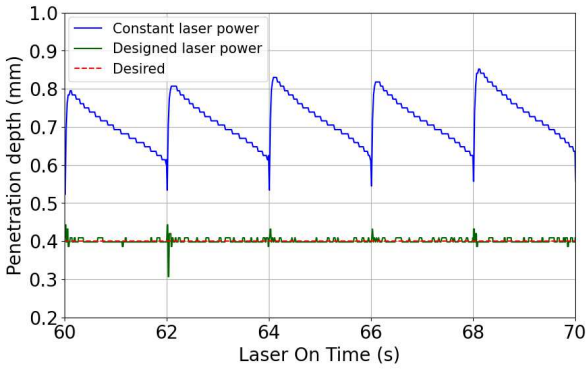
Figure 4: (a) Bidirectional wall dimensions with scanning sequence, (b) adaptive mesh refinement for the FE analysis



(a)



(b)



(c)

Figure 5: (a) Designed laser power profile, (b) simulation results of the bidirectional wall, (c) penetration depth of the laser against time

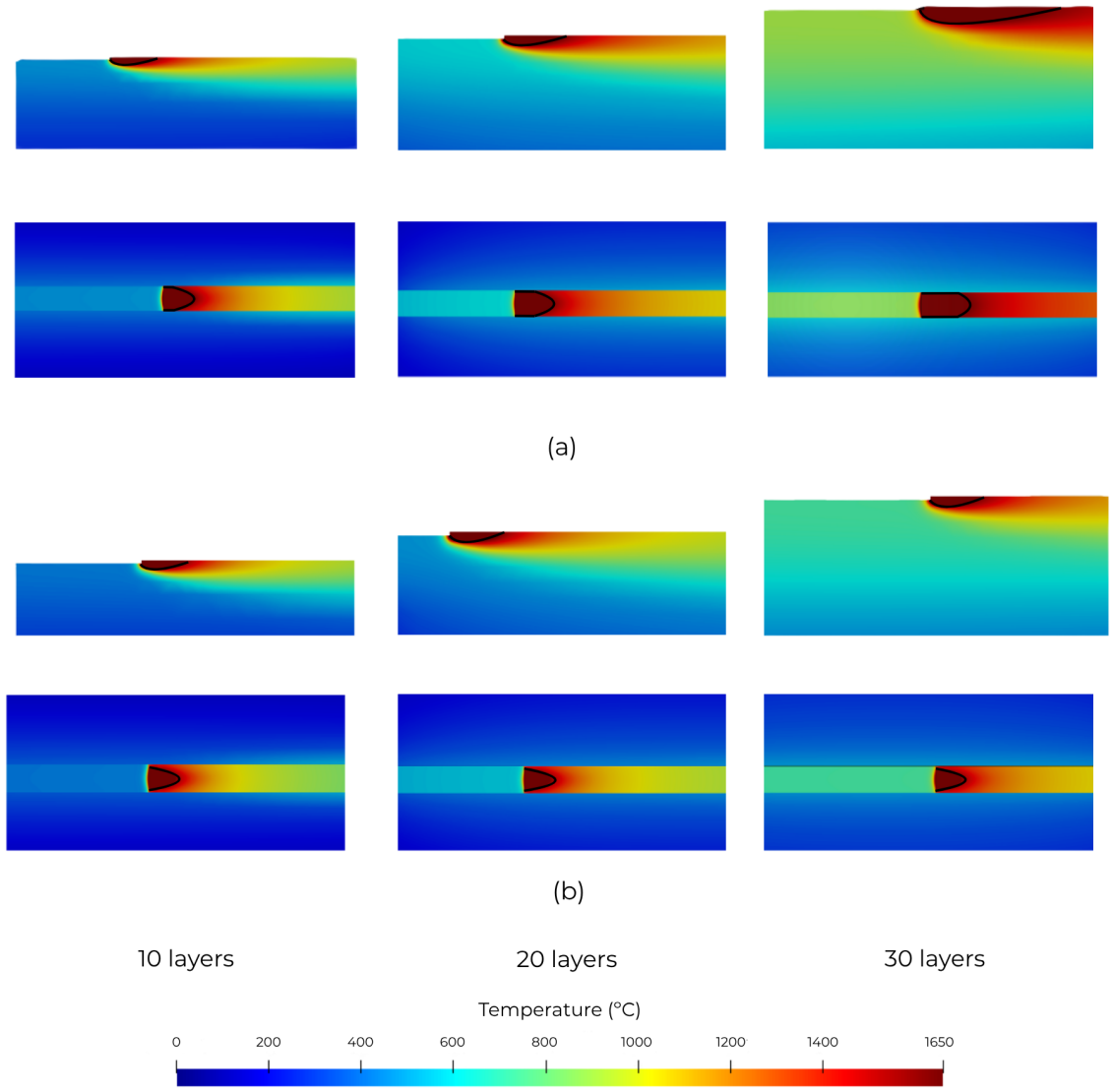


Figure 6: Visualization of the temperature field and the outline of the melt pool in the simulation (a) without control, (b) with control.

2.3 AI-based power control

Penetration depth (D) was selected as the criterion for the offline a-posteriori optimization to improve the buildability of the printed part and also to enable the generation of a representative dataset for the training of the ML model. The simulated cases comprise of solid single-hatch thin walls being deposited in a unidirectional and bidirectional scanning sequence ranging from 10 mm to 110 mm in 5 mm increments. This accounts for 42 simulated cases providing a solid dataset for the robust training and generalization abilities of the neural network developed.

2.3.1 Synthetic data correlation analysis

The simulated data includes a range of information from deposition temperatures to the geometric dimensions of the melt pool, as illustrated in Figure 7. A Spearman's rank correlation coefficient matrix was developed to avoid unselectively using all simulated results and overfitting of the ANN. This approach was selected because it focuses on the monotonic relationship between paired data, rather than their

actual values, enhancing robustness to outliers and non-normally distributed data. Coefficient values approaching -1 indicate a significant negative monotonic relationship, while those close to 1 indicate a substantial positive monotonic relationship between the paired features. Spearman's coefficient (ρ) is defined by:

$$\rho = 1 - \frac{6\sum_{i=1}^{n} d_i^2}{n^3 - n} \tag{5}$$

where d_i represents the difference between the ranked paired features and n is the number of observations [36]. A strong and very strong correlation between paired variables is indicated by an absolute value of $\rho \geq 0.6$ and $\rho \geq 0.8$, respectively [37]. To acquire data for the correlation analysis, a total of 30 samples of single tracks were simulated, with the power supply systematically varied from 1000 W to 2000 W in increments of 200 W. Furthermore, the substrate temperature was adjusted to replicate various stages of the printing process, specifically at 20 °C, 100 °C, 500 °C, 800 °C, and 1000 °C.

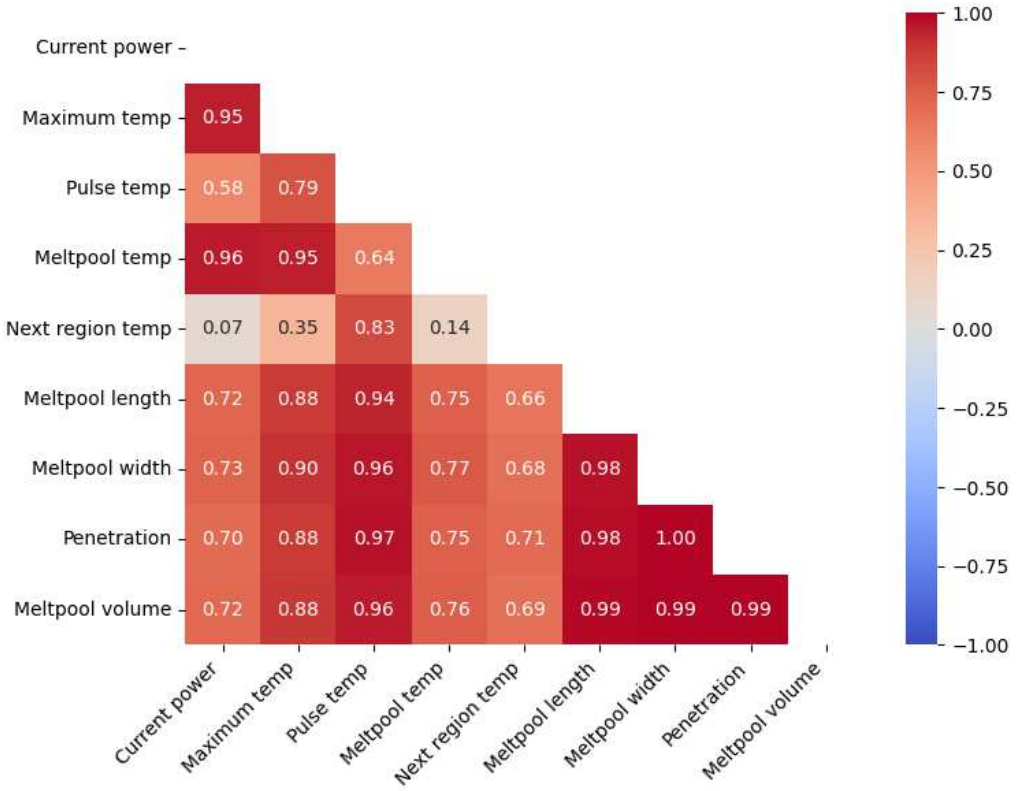


Figure 7: Spearman's rank correlation coefficient map for each simulated variable pair

Figure 7 illustrates the influence of the laser power supply on the simulated parameters, with the most influenced ones are the maximum temperature and the melt pool temperature, defined as the highest temperature attained within the monitored domain and the spatially averaged temperature over the molten region, respectively. The pulse temperature, defined as the temperature in the monitored domain immediately after each individual power input pulse, is also included as a key input feature of the ML model, as it characterizes the thermal energy delivered to the system. The next region temperature, representing the temperature at a distance of one step size ahead of the current laser position, exhibits a strong correlation of 0.71 with the penetration depth, highlighting its crucial role as an input feature for monitoring purposes. Incorporating the temperature of the next deposition region as an input feature may enhance the ability of the ML algorithm to understand the scanning sequence. Such information is particularly relevant when addressing complex scanning scenarios, aiding the ML model in distinguishing between various scanning sequences, such as corners, unidirectional versus bidirectional walls, or complex patterns, e.g. a partition infill of a structural part. Similarly, geometric characteristics, including melt pool length, melt pool volume, and penetration depth, exhibit strong correlations with the power supply,

making them essential input features for the ML model. An additional input feature included in the ML model is the melt pool penetration depth of the next region. To incorporate this parameter into the training of the ML model, the dataset is reorganized so that the penetration at the next time step is appended as an input feature to the current time step. Thus, each data record for a given step includes both the current penetration depth and the penetration depth at the subsequent step. This feature is not included in the correlation analysis, as it is introduced primarily as a safeguard for the ML-based surrogate controller and because it is not available during run-time control, it is pre-emptively set to the target penetration depth of 0.40 mm. In this way, the ML model explicitly incorporates the penetration-depth criterion when evaluating corrective power values, ensuring that the predicted laser power reflects both the current deposition state and the desired penetration at the subsequent time step.

2.3.2 Neural network architecture

The effectiveness of ML models is enhanced through the fine-tuning of *hyperparameters*, which define the architecture of the model. Among various hyperparameter tuning techniques, Bayesian optimization has garnered significant attention due to its capability to optimize objective functions that are costly to evaluate. This method utilizes a Gaussian process regression to probabilistically model the objective function, effectively capturing uncertainty regarding its values. An acquisition function, such as expected improvement, directs the selection of subsequent sample points by balancing the exploration of uncertain regions with the exploitation of areas anticipated to yield high values. This iterative procedure updates the model with new data, progressively refining the search for the global optimum, making it particularly suitable for scenarios where function evaluations are expensive or time-consuming [38]. Consequently, employing a Bayesian optimization approach within the *Keras* libraries [39] allows a comprehensive search of the optimal hyperparameters tailored for the ML model, aimed at optimizing the power variation of the laser during the deposition process, as outlined in Table 3. The final architecture designed along with the informative selection of input features, is summarized in Figure 8(a).

Table 3: Selection of hyperparameters

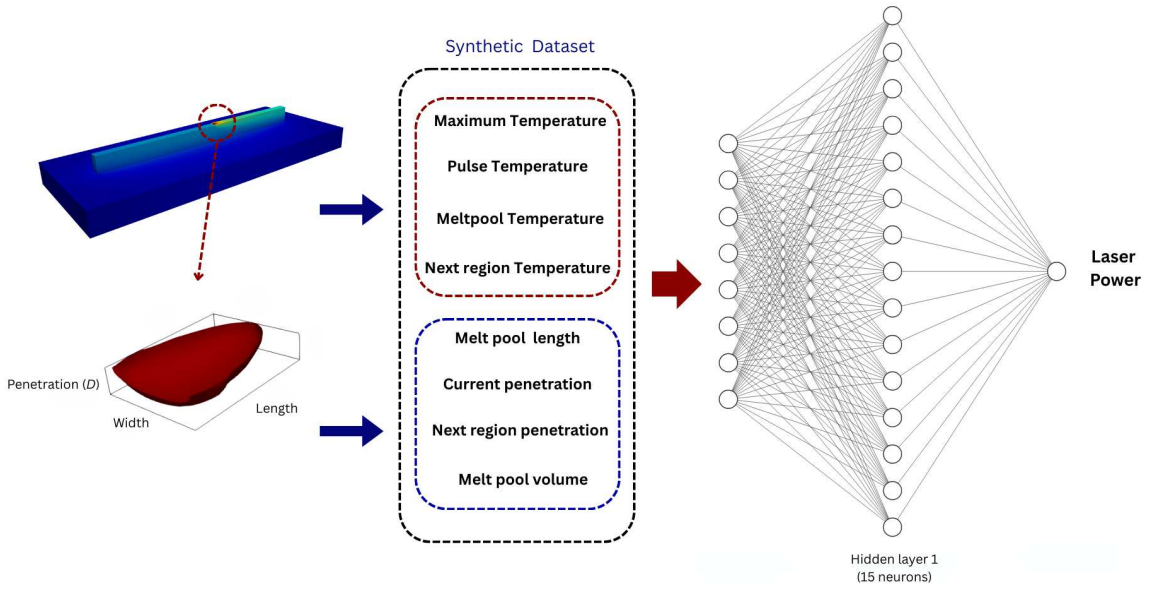
Hyperparameter	**Range**	**Selected**
Layer	1 - 2	1
Neurons	Min: 5 Max: 50 Step: 5	15
Activation functions	ReLU [40], Leaky ReLU [41]	ReLU
Learning Rate	Min: 1e-4 Median: 1e-3 Max: 1e-2	1e-3
Loss function	Mean squared error (MSE), Mean absolute error (MAE)	Mean absolute error

The Adaptive Moment Estimation (*Adam*) algorithm was selected for the stochastic gradient descent process due to its robust capabilities to adapt to combinations of hyperparameters and faster convergence [42]. A learning rate of 1×10^{-3} was carefully selected, accounting for stability during the search of local minima of the loss function and ensuring a convergence speed fast enough during the training process. This allowed the model to be trained with as much data as possible without sacrificing precision. Early stopping was employed as a regularization technique to prevent overfitting of data during the training phase. A patience parameter of 20 epochs was set to determine the continuation of training after the last observed improvement in validation performance. This ensures adequate training and minimizes the risk of the model learning spurious relationships, leading to a degradation in the performance of the model. The data was normalized across each feature to enhance computational

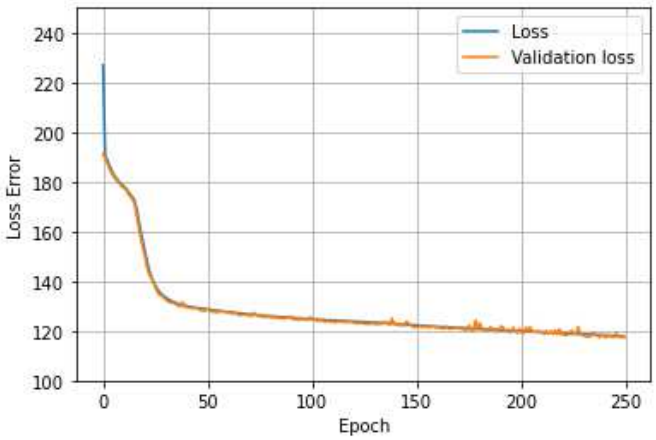
stability and improve convergence of the training process. The scaled dataset was then split into a training set (80%) and a validation set (20%) which is a common standard and a fivefold cross-validation approach was applied during the training process. MAE was adopted as the loss function governing the training of the ML model because it is less sensitive to outliers than MSE. A small number of large deviations in the synthetic data at specific scan-path segments would be over-emphasized by MSE, potentially biasing the model towards these regions at the expense of overall consistency. In contrast, MAE provides a more robust criterion for training the surrogate controller across the entire deposition process and is defined as:

$$\mathrm{LOSS}(P, \hat{P}) = \frac{1}{\widetilde{n}} \sum_{j=1}^{\widetilde{n}} \left| P_j - \hat{P}_j \right| \tag{6}$$

where P represents the actual power, $\hat{P}$ the predicted power and $\widetilde{n}$ is the number of data points. Figure 8(b) illustrates the training process of the ML model showing the training and validation loss curves. Initially, both curves decrease sharply, indicating rapid learning and effective parameter adjustments. As training progresses, the curves gradually converge, demonstrating that the model learns efficiently without significant overfitting. In the final phase, the curves plateau, showing diminishing returns in performance improvement. Early stopping terminated the training process at 250 epochs, ensuring the model did not overfit and maintained good generalization to unseen data.



(a)



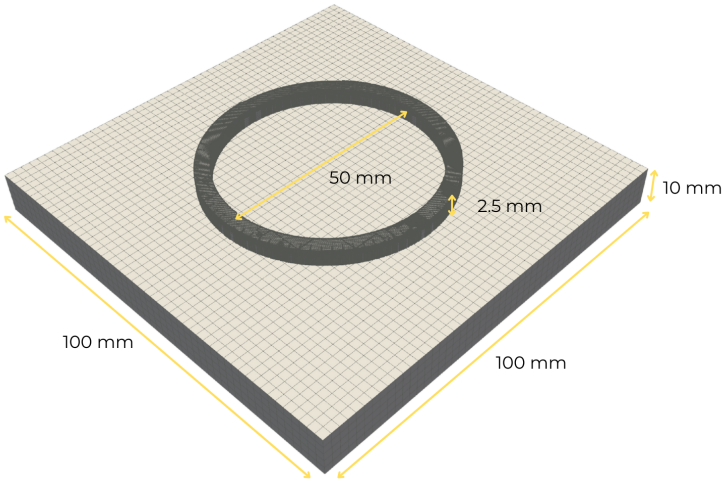
(b)

Figure 8: (a) Schematic of the optimized R-ANN architecture developed with selected input features for optimal power predictions, (b) loss curves illustrating the training process of the ML model.

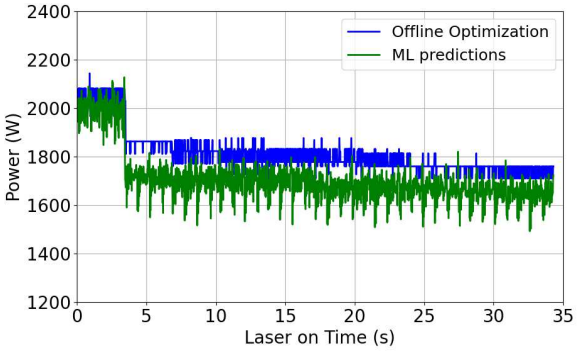
2.3.3 Validation of the ML model

The robust generalization capability of the developed ML model was demonstrated by validating it on an unseen deposition sequence as shown in Figure 9(a). The processing parameters used for the optimization of the cylinder are similar to the bidirectional wall described in section 2.2.1 and tabulated in Table 2. The mesh consists of 594,890 hexahedral 8-noded elements and 791,529 nodes, while the simulation consists of 1719 time-steps with $\Delta t = 0.02$ s. Once the offline optimization process is completed, the optimized synthetic dataset consisting of the thermal profiles and geometric signatures of the melt pool is used to evaluate the power predictions of the ML model. Figure 9(b) presents a comparison between the offline-optimized power supply and the power values predicted by the ML model. Figure 9(c) presents the error in the power values between the offline optimization and the ML predictions, assessed using 4 different metrics as illustrated in Table 4. The ML model exhibits strong predictive capabilities, achieving an

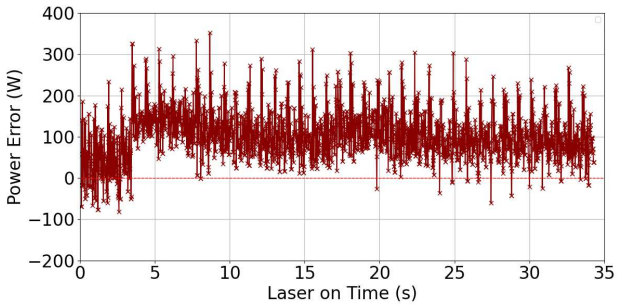
MAE of 100.4 W and an MAPE of 5.55 %. These results are noteworthy given that the model was tested on an untrained case, and the MAE obtained is reasonably appropriate for power processing windows in the range of 1700 W - 2000 W. The ML predictions were generated within the first iteration, whereas the offline optimization took 6 iterations, resulting in significant resource savings. This enhanced prediction capability indicates a significantly faster determination of the optimal power supply, thereby improving prototyping capabilities. After validating the ML model in an offline setup, the latter is deployed in a computational environment to control the laser power during the run-time of the simulation, as described in the following section.



(a)



(b)



(c)

Figure 9: (a) Representation of the validation case with dimensions, (b) comparison of the optimal power supply for the printing of the cylinder between the offline optimization approach and ML predictions, (c) power error between the offline optimization and ML predictions during the deposition process.

Table 4: Evaluation of power error between the offline optimization approach and ML predictions for the validation case.

Error metric	Value
Mean absolute error (MAE) [W]	100.40
Maximum absolute error (MXAE) [W]	352.60
Mean absolute percentage error (MAPE) [%]	5.55
Maximum absolute percentage error (MXAPE) [%]	18.88

2.3.4 Virtual integration of the ML model with the FE solver

The control strategy utilizes the developed ML model within a closed loop alongside the in-house FE solver FEMUSS, developed in an object-oriented framework based on Fortran-2008 and integrated with the Python library *Forpy* to enable Fortran-Python interoperability [43]. The measured and selected physical quantities from the simulations are fed into the ML as input features, which are then analyzed to output a corrective power supply, controlling and maintaining a constant penetration depth (D) of 0.40 mm. This approach establishes a control strategy capable of managing dynamic fluctuations in both the deposition temperature and the dimensional parameters of the melt pool throughout the printing process, thus providing a run-time control system without any human intervention, as summarized in Figure 10.

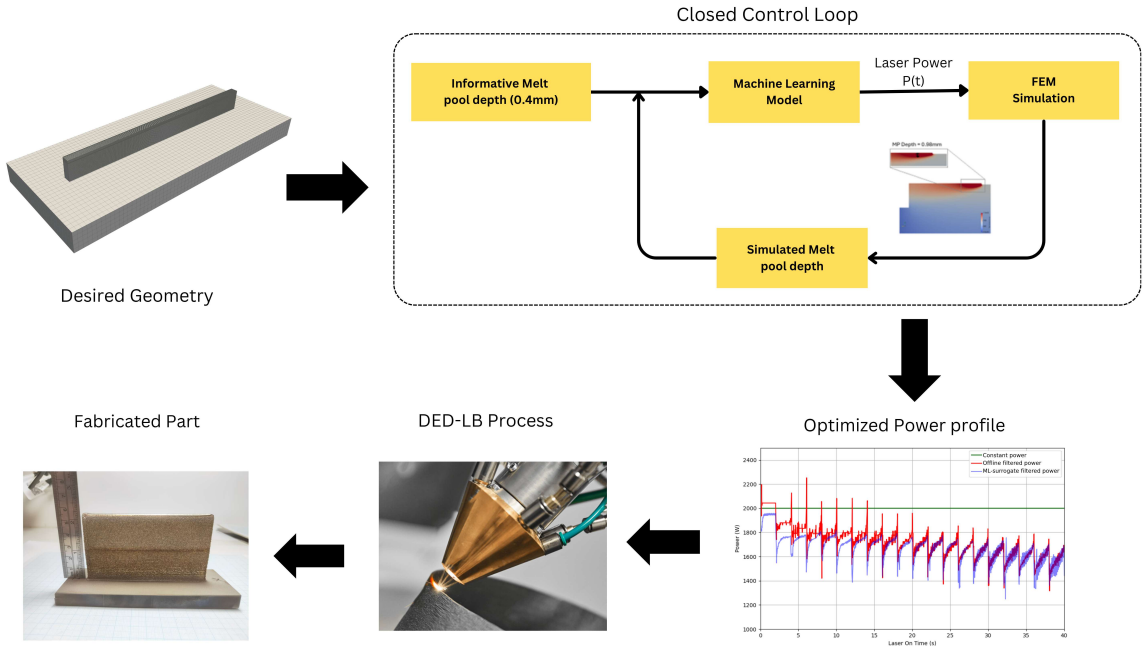


Figure 10: Procedure of integrating the ML model with the FE solver forming a closed control loop. Adapted from [4].

3 Numerical Examples

In this section, the developed control environment of DED-LB was assessed on three example cases, i.e., a unidirectional thin wall, a hollow, and an infill-partitioned cubic deposition scanning sequence, aiming to maintain the melt pool penetration depth at 0.40 mm by varying the power supply of the laser. The material used for the tests is titanium alloy Ti-6Al-4V, and the temperature-dependent properties used in the simulations can be found in [35]. A detailed description of the cases and their simulation results are presented as follows.

3.1 Case 1: Unidirectional thin wall

A thin wall of length 100 mm and a height of 5 mm (20 layers of 0.25 mm) following a unidirectional scanning sequence was used as the first comparative case, as shown in Figure 11. The offline optimization was conducted on a High-Performance Computer (HPC) cluster using 16 processors and 5 iterations, to identify the optimal power profile and took approximately 40 hours of computational time. The ML-based surrogate control strategy was conducted on the same computational architecture, and 1 iteration, lasting approximately 12 hours, making it roughly 3 times faster than the offline optimization. The mesh consists of 210,828 hexahedral 8-noded elements and 301,945 nodes, while the simulation consists of 3998

time-steps with $\Delta t = 0.02$ s. The HTCs values and processing parameters used for the optimization of the thin wall are similar to those illustrated in Table 1 and Table 2, respectively. A unidirectional toolpath consists of the laser promptly returning to the original deposition point and starts to build the next layer once the current one is completed.

Figure 12 (a) presents the three different power strategies, and filtering the power profiles with a simple moving average, it can be observed that the ML-based surrogate approach identified the correct pattern for the power reduction. This results in a precisely controlled melt pool penetration depth as shown in Figure 12 (b) and (c). A small window size for the moving average ensures responsiveness while effectively smoothing short-term fluctuations in power demand. In the context of the dynamic nature of AM processes, which requires visualizing short-term fluctuations of the power, a window size of 10 data points is chosen. The study by [44] highlights the significance of monitoring both the melt pool depth and length, as these interrelated dimensions influence the overall melt pool profile. Figure 12 (d) presents a comparison of the melt pool length across the different power strategies. Along the printing process, it can be concluded that when a constant power is maintained, the melt pool depth tends to grow uncontrollably, therefore, there is the need to design a power profile accounting for the regulation of thermal energy supplied. Similarly, in the absence of power control, the melt pool length increases significantly. In contrast, the ML-based surrogate control strategy maintains the melt pool length within the same range as the offline optimization, as shown in Figure 12 (e). It can also be observed that the melt pool length grows smoother to the target value in the ML-surrogate control approach as compared to the two other power strategies, promoting stability of the melt pool morphology.

As noted in [45], the printability of alloys often involves multiple heuristic stages in which processing parameters such as laser power are adjusted experimentally through trial and error until an acceptable geometric accuracy is achieved. In contrast, performing a full FE optimization of the processing parameters is highly computationally intensive. Given the close agreement in melt-pool morphology and the substantially reduced computation time, the ML-based surrogate control framework offers enhanced capabilities for rapid prototyping and facilitates the manufacture of high-productivity AM parts.

Currently, the proposed strategy is implemented as a single-parameter control scheme to evaluate the feasibility of the developed ML-based surrogate control framework. Nonetheless, the approach can be extended to a multi-objective control framework that includes simultaneous adjustment of powder feed rate. As reported in [46], inadequate regulation of high powder feed rates can increase surface roughness owing to incomplete melting of excess powder. In addition, if the powder feed rate is not reduced when the laser power is decreased, unmelted powder may adhere to the heated wall, thereby degrading the resulting surface quality.

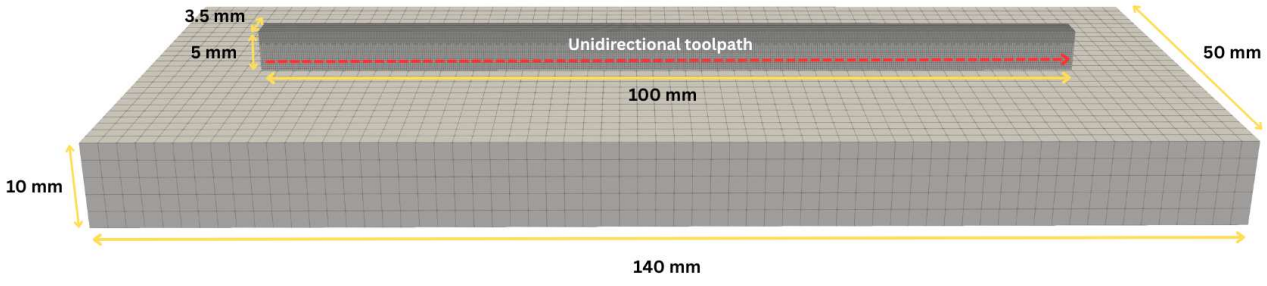


Figure 11: Unidirectional wall dimensions with scanning sequence.

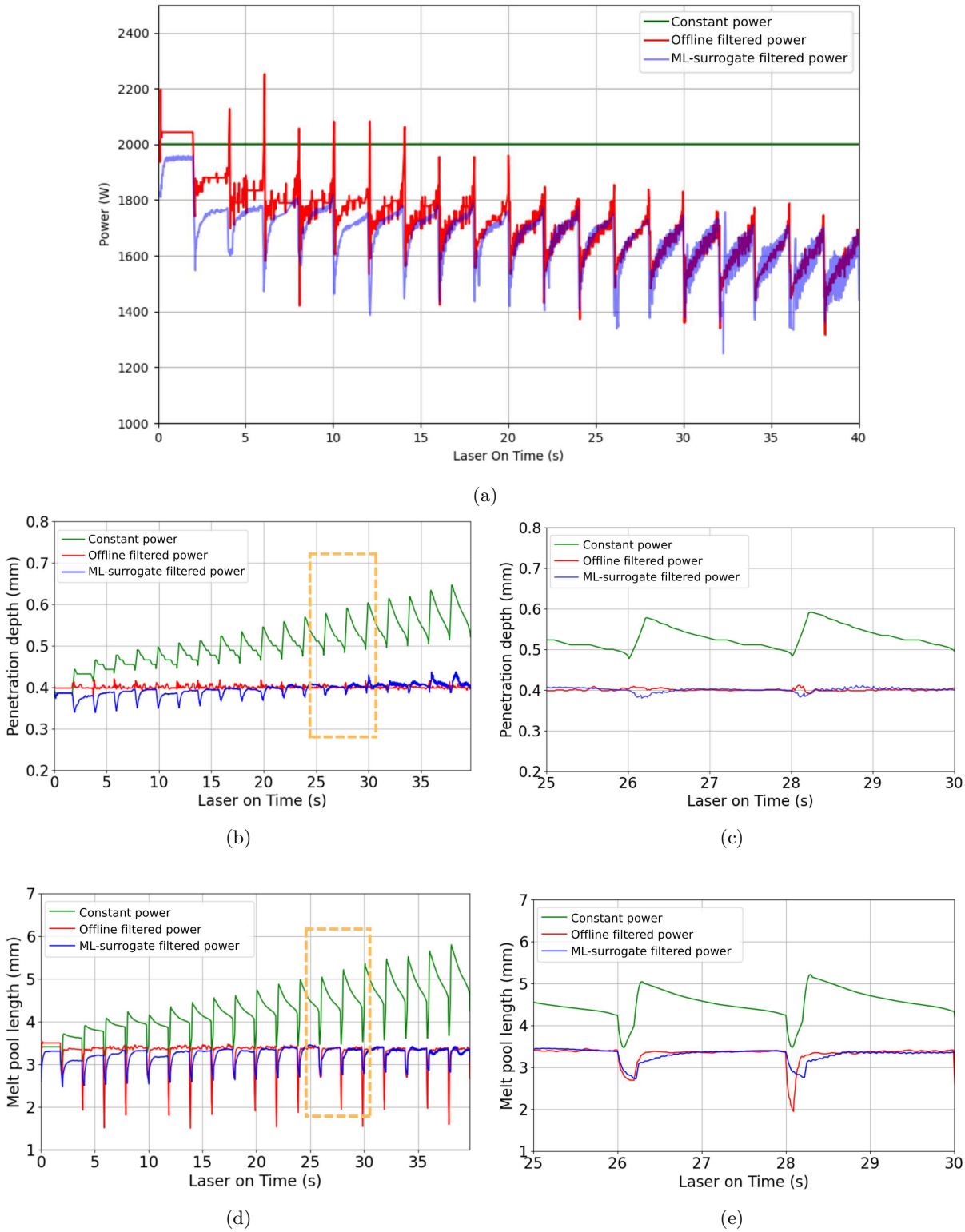


Figure 12: Unidirectional thin wall: (a) Time-series power profiles, (b) simulation results of the penetration depth, (c) monitoring of the penetration depth, (d) simulation results of the melt pool length, (e) monitoring of the melt pool length.

Figure 13 demonstrates the evolution of the melt pool for the printing of a hatch for the unidirectional wall using the offline optimization strategy and ML-based surrogate control approach. It can

be observed that an almost constant melt pool height is maintained throughout the printing of the hatch for both strategies, which consists of the layer height ($h_0 = 0.25$ mm) and the desired penetration depth ($D_{target} = 0.40$ mm), resulting in a targeted height of 0.65 mm. Also, as mentioned before, it can be observed that the transition in temperatures is smoother for the ML-based surrogate control strategy as compared to the offline optimization strategy at the beginning of the hatch, therefore, enhancing melt pool length stability.

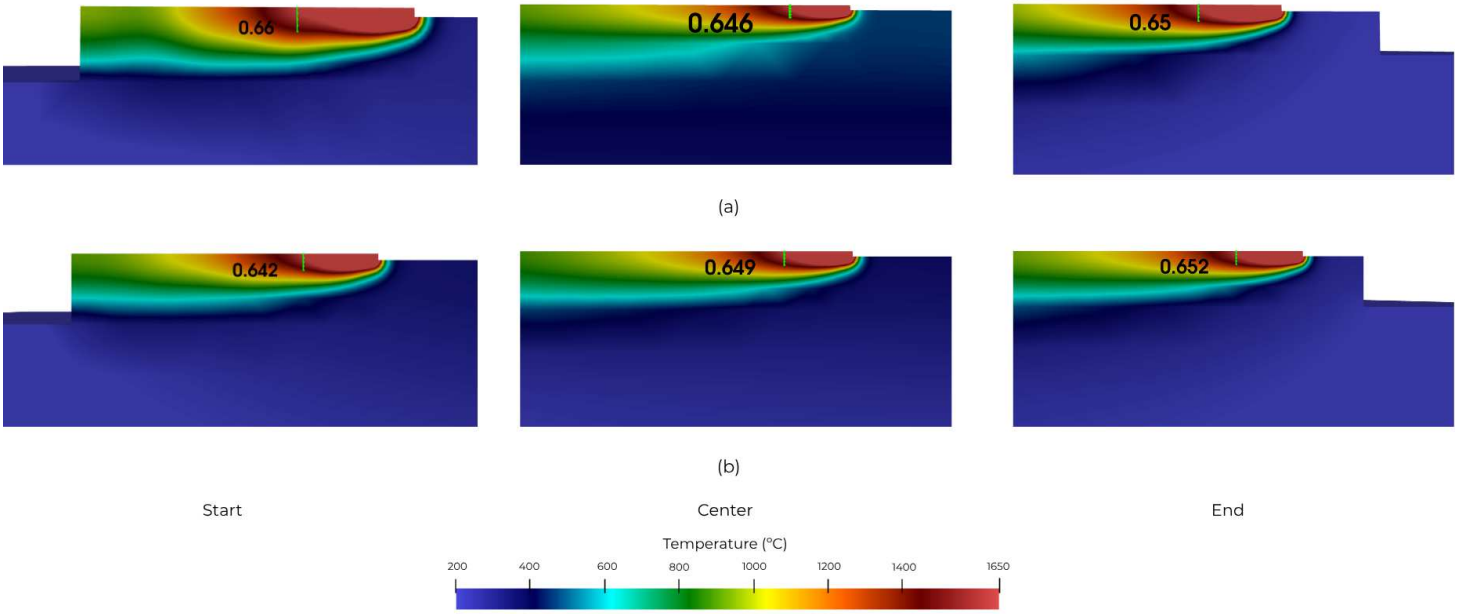


Figure 13: Contour plots showing the melt pool height in millimeters (a) for the offline optimization strategy, (b) and the ML-surrogate control strategy.

3.2 Case 2: Hollow cubic deposition

The second test is a hollow cubic deposition of length 80 mm and 10 mm in height (40 layers of 0.25 mm) as shown in Figure 14. The offline optimization was conducted on an HPC cluster using 52 processors and 3 iterations, to identify the optimal power profile and took approximately 141 hours of computational time. The ML-based surrogate control strategy was conducted using the same computational architecture, and 1 iteration, lasting approximately 57 hours, making it almost 2.5 times faster than the offline optimization. The mesh consists of 2,030,080 hexahedral 8-noded elements and 2,353,538 nodes, while the simulation consists of 17,464 time-steps with $\Delta t = 0.02$ s. The HTCs values and processing parameters used for the optimization of the cubic deposition are tabulated in Table 1 and Table 2, respectively.

Figure 15 (a) presents the designed power profiles from the offline optimization and ML-based surrogate control approaches. The latter achieved a power reduction profile similar to the offline method, effectively minimizing heat accumulation throughout the deposition process. Figure 16 illustrates a spatial analysis of the historical power variation observed during the printing process. The plots reveal that both the offline optimization and ML-based surrogate control strategies exhibit similar distinct regions of power reduction. Notably, the ML-based surrogate strategy shows a higher degree of fluctuation in power variation, indicating that further post-modulation of power may be necessary to maintain deposition stability throughout the printing process.

As shown in the previous case, with a constant laser power supply, both the melt pool penetration depth and length increase uncontrollably. In contrast, the melt pool penetration depth and length remain relatively constant for both the offline and ML-based surrogate approaches as illustrated in Figure 15 (b) and (d). The contour plot in Figure 17 further demonstrates that under a constant laser power supply, the melt pool penetration depth increased rapidly. On the other hand, both the offline optimization and ML-surrogate control strategies kept the melt pool penetration depth within an almost constant range during the deposition process. However, an increase in penetration depth is observed for both strategies when the laser transitions between hatches, due to localized heat accumulation. This observation suggests

that introducing a cooling period might be necessary to reduce the temperature to a controlled residual level before starting the next hatch. A statistical analysis was conducted to assess the uniformity of the deposition process. The mean value of the offline melt pool morphology, i.e. the penetration depth and length, is taken as the reference. According to [45], maintaining structural integrity and quality of an AM component requires rigorous monitoring of the melt pool formation thus, an interval of 10 % from the reference value is assumed to be within the desired process window. Table 5 provides the statistical assessment of the melt pool morphology for the 3 power strategies with respect to the reference morphology. The density plots reveal the distribution of the melt pool characteristics for each approach, as shown in Figure 15 (c) and (e). It can be observed that the ML-based surrogate controller maintains a precise preservation of the melt pool morphology throughout the deposition process when compared to the offline optimization approach, highlighting the superior quality of the surrogate counterpart. For instance, 98.51 % of the penetration depth is distributed across 10 % of 0.40 mm for the offline optimization, 91.77 % for the ML-based surrogate control, and only 1.13 % for the constant laser power supply. This demonstrates the superior quality of the ML-accelerated processing-parameter planning achieved by the ML-based surrogate controller.

The ML model trained on HF simulated data was able to predict accurately a deposition sequence that it was not trained on, therefore demonstrating the robustness of the generalization ability of the model. This capability provides a reliable initial identification of the power processing parameter window for printing new structural parts, thereby enhancing prototyping abilities for complex AM components.

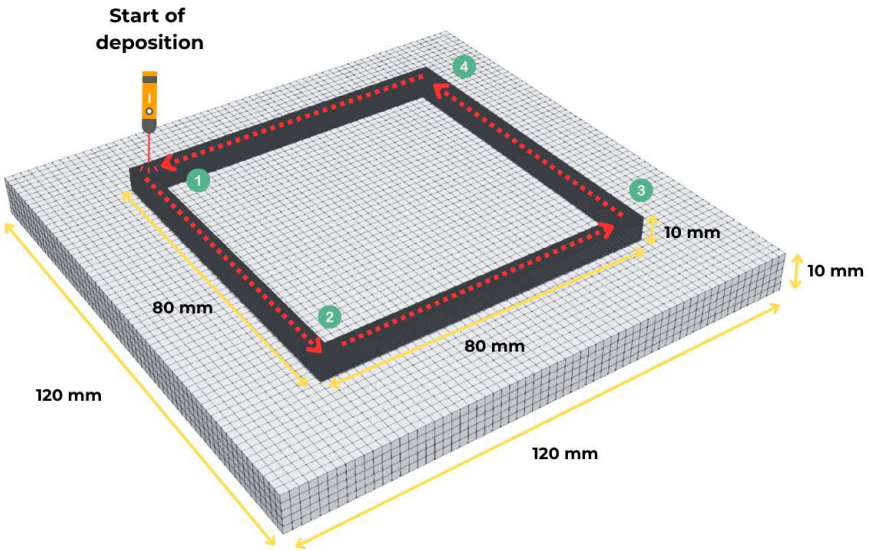
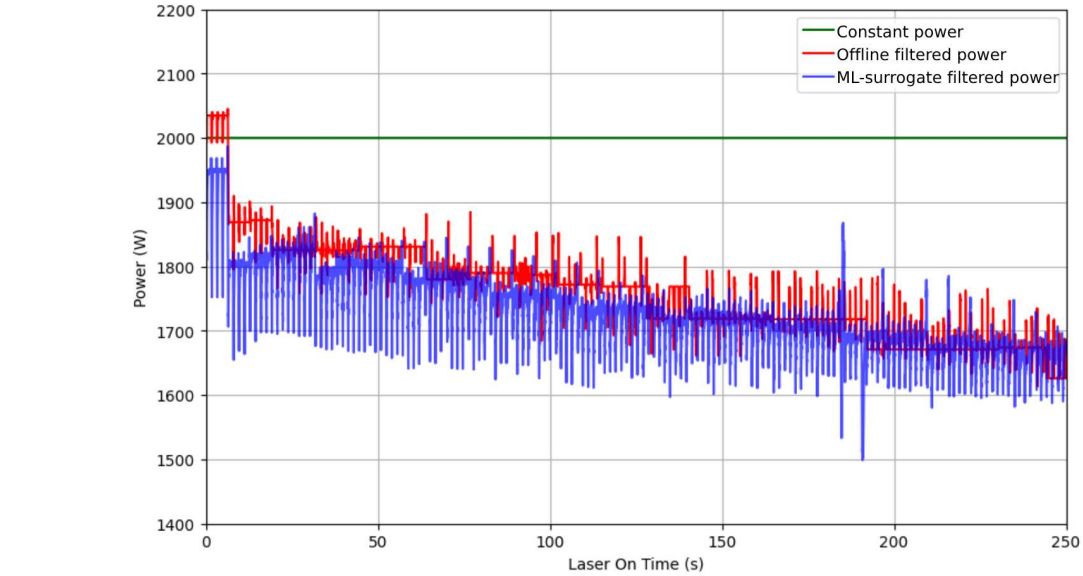
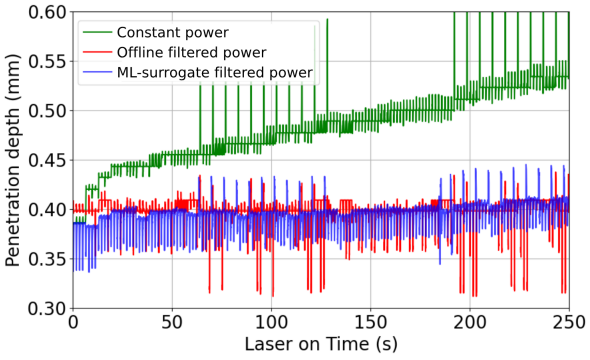


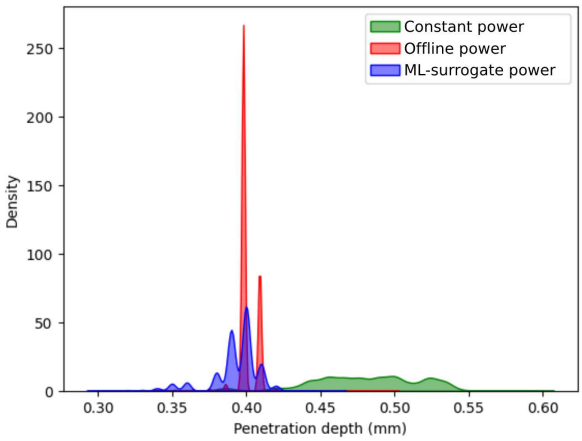
Figure 14: Hollow cubic deposition: Dimensions and scanning sequence.



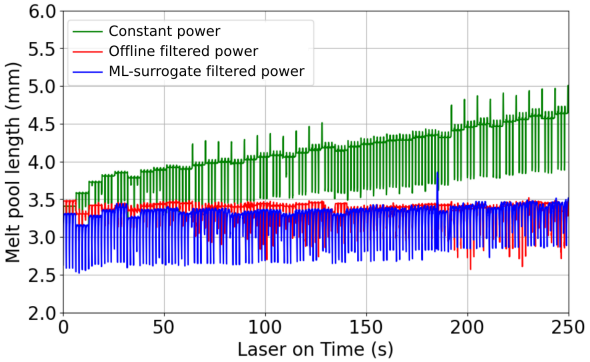
(a)



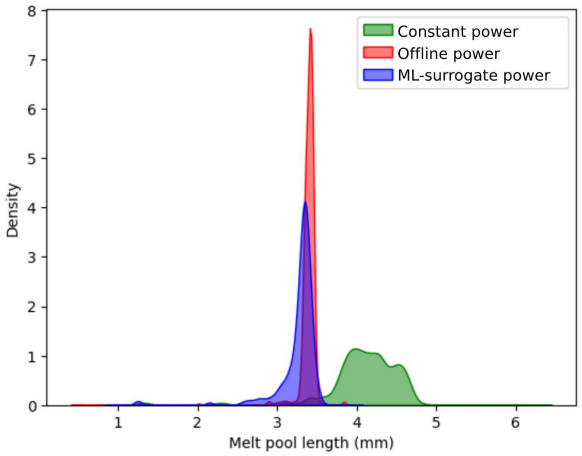
(b)



(c)

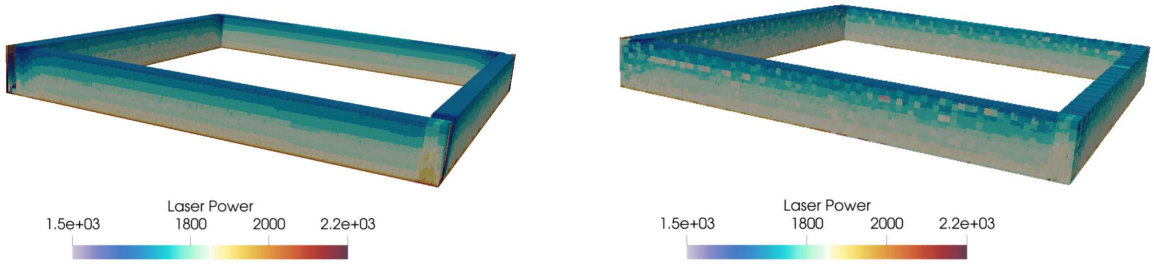


(d)



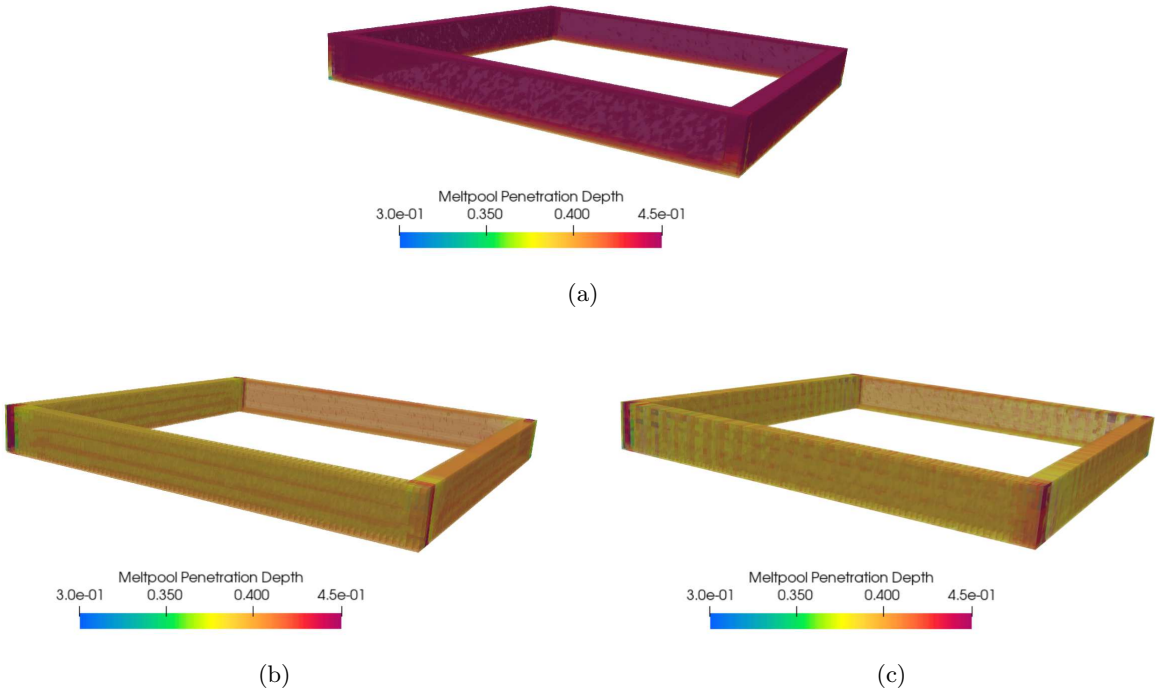
(e)

Figure 15: Hollow cubic deposition: (a) Time-series power profiles, (b) simulation results of the penetration depth, (c) density plot illustrating the distribution of the penetration depth, (d) simulation results of the melt pool length, (e) density plot illustrating the distribution of the melt pool length.



(a) (b)

Figure 16: History contour plot of the power supply for the: (a) offline optimization, (b) ML-based surrogate control.



(a)

(b) (c)

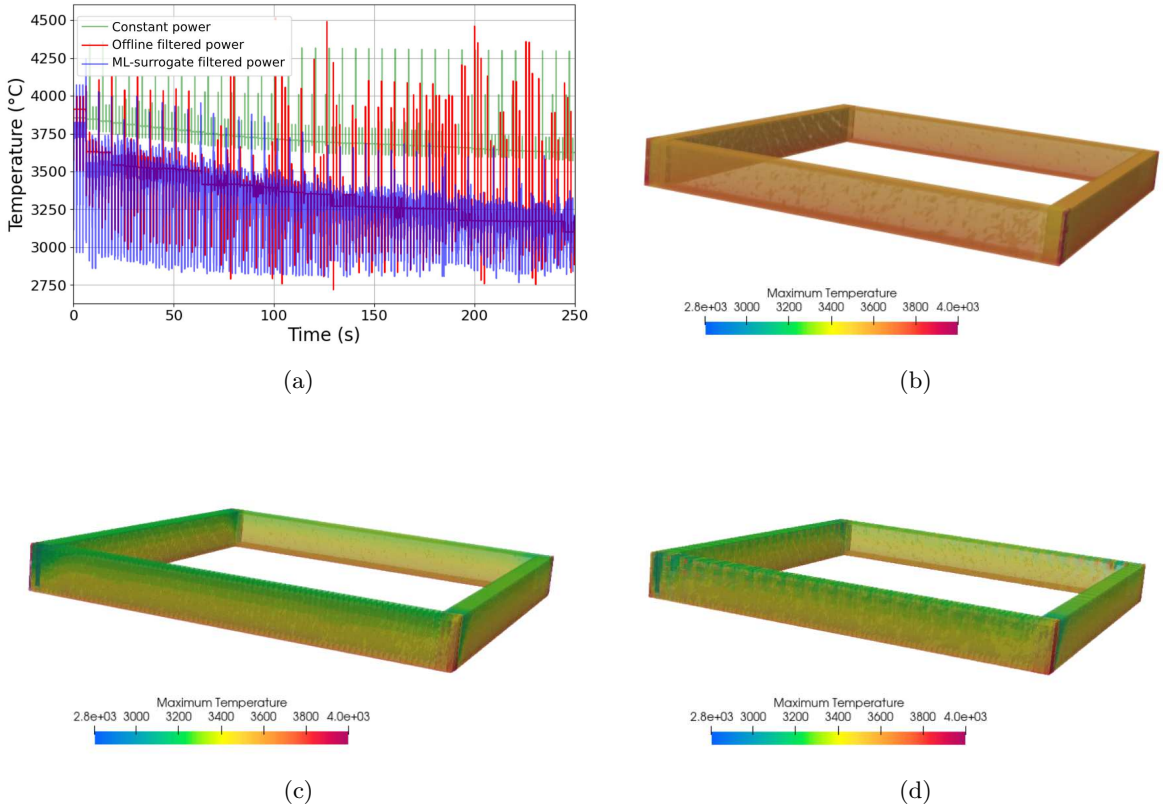
Figure 17: History contour plot of the melt pool penetration depth for the: (a) constant power supply, (b) offline optimization, (c) ML-based surrogate control.

Table 5: Melt pool characteristics based on different power strategies.

Criteria	Constant power/ %	Offline designed power/ %	ML-surrogate designed power/ %
Penetration depth (0.38 mm - 0.42 mm)	1.13	98.51	91.77
Melt pool length (3.21 mm - 3.55 mm)	0.31	96.11	82.81

The evolution of the maximum temperature during the deposition process was analyzed, and Figure 18 (a) illustrates that both the offline optimization and ML-based surrogate control strategies achieve the necessary temperature minimization at a consistent trend. In contrast, the constant power strategy leads to elevated maximum temperature values throughout the deposition process. Contour

plots showing the maximum temperature history during the printing process were used to visualize the temperature evolution. Figure 18 (b) indicates sustained high temperatures during the printing process when using a constant laser supply. On the contrary, both the offline optimization and ML-based surrogate control power strategies, depicted in Figure 18 (c) and (d), demonstrate a reduction in thermal accumulation during the printing process, thereby stabilizing the melt pool morphology by preventing excessive melt pool growth and overheating-induced instabilities such as keyholing. It can also be noted that the base layers exhibit higher temperatures due to their initial deposition at elevated power levels and continuous exposure to subsequent thermal cycles, resulting in heat accumulation at the bottom. Additionally, the upper layers cool more rapidly due to environmental exposure and convection effects.



(a) (b)

(c) (d)

Figure 18: (a) Maximum temperature evolution throughout the deposition process and corresponding contour plots for the: (b) constant power supply, (c) offline optimization, (d) ML-based surrogate control.

3.3 Case 3: Infill-partitioned cubic deposition

A third geometry was tested to demonstrate the versatility of the ML model developed, which is a cubic deposition with an infill partition of length 80 mm and height 10 mm (25 layers of 0.25 mm), as illustrated in Figure 19. A continuous scanning sequence was selected, as per [47] it ensures that the thermal gradient within the melt pool remains consistent, thereby controlling the cooling rates and preventing the formation of defects such as porosity or cracks, especially at the edges. The offline optimization was conducted on an HPC cluster using 48 processors and 3 iterations, to identify the optimal power profile and took approximately 174 hours of computational time. The ML-based surrogate control strategy was conducted using the same computational architecture, and 1 iteration, lasting approximately 58 hours, making it 3 times faster than the offline optimization. The mesh consists of 1,229,716 hexahedral 8-noded elements and 1,497,573 nodes, while the simulation consists of 13,045 time-steps with $\Delta t = 0.02$ s. The HTCs values and processing parameters used for the optimization of the infill-partitioned cubic deposition are tabulated in Table 1 and Table 2, respectively.

Figure 20 (a) presents the designed power profiles from the offline and ML-based surrogate control approaches. It can be observed that the latter could establish the power reduction expected throughout the deposition process, to minimize heat accumulation, similarly to the offline optimization.

The melt pool penetration depth and length remain relatively constant for both the offline optimization and ML-based surrogate control approaches as illustrated in Figure 20 (b) and (d). In contrast, with a constant laser power supply, both the penetration depth and melt pool length increase uncontrollably, as demonstrated in previous cases.

Through the density plots shown in Figure 20 (c) and (e), the melt pool penetration depth and length are bounded mostly within the same range for both the offline optimization and ML-based surrogate control approaches. For instance, 96.43 % of the penetration depth is distributed within 0.38 mm - 0.42 mm for the offline optimization, 87.68 % for the ML-based surrogate control and only 1.13 % for the constant laser power supply, as presented in Table 6. In addition to that, the melt pool length is stabilized to a greater extent during the ML-based surrogate control rather than the offline optimization approach, with 84.64 % of the melt pool length within 3.18 mm - 3.52 mm for the offline optimization and 87.54 % for the ML-based surrogate control. This reiterates the strict control of the melt pool morphology provided by the ML-enhanced framework on another scanning sequence not included in its training dataset.

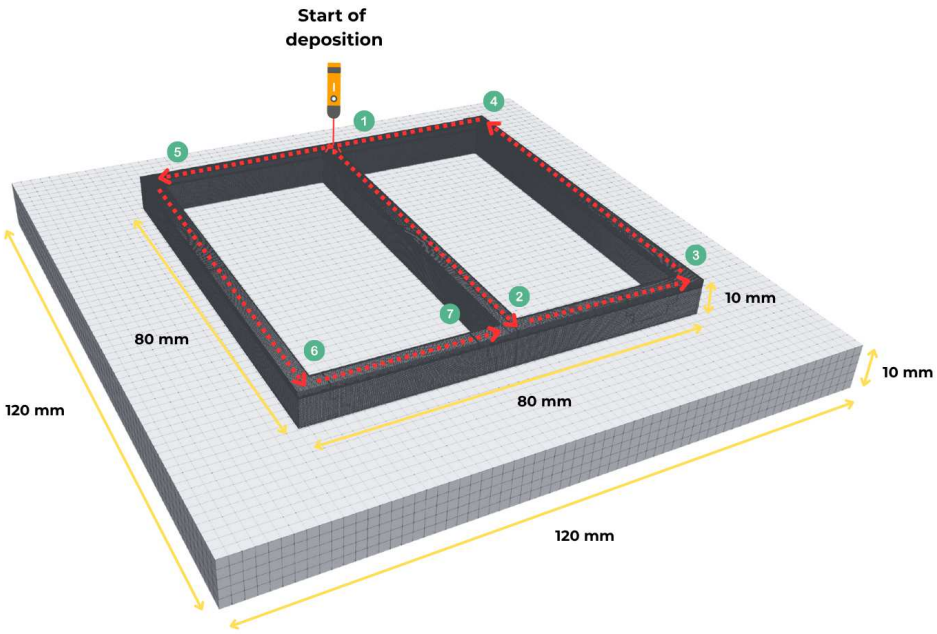
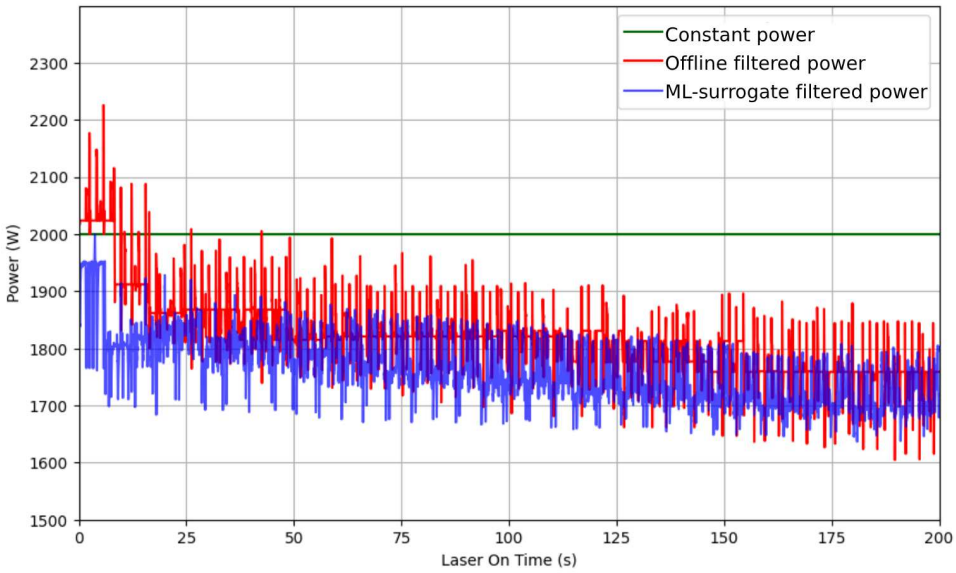
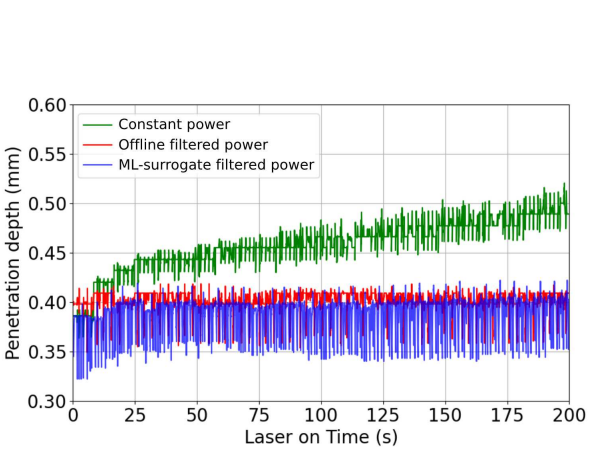


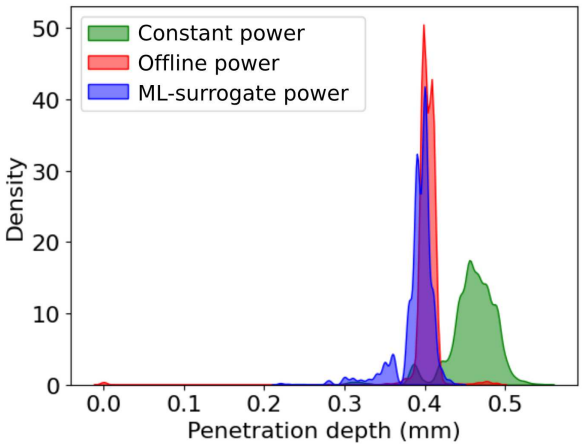
Figure 19: Infill-partitioned cubic deposition: Dimensions and scanning sequence.



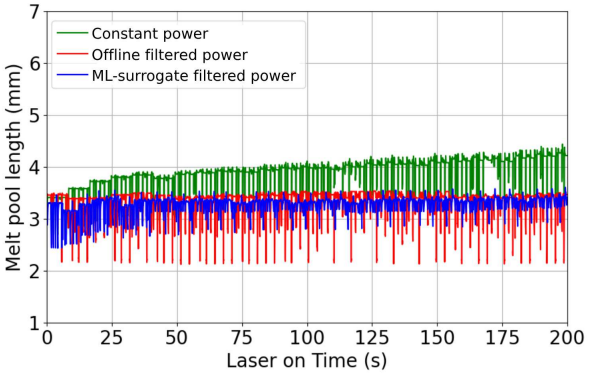
(a)



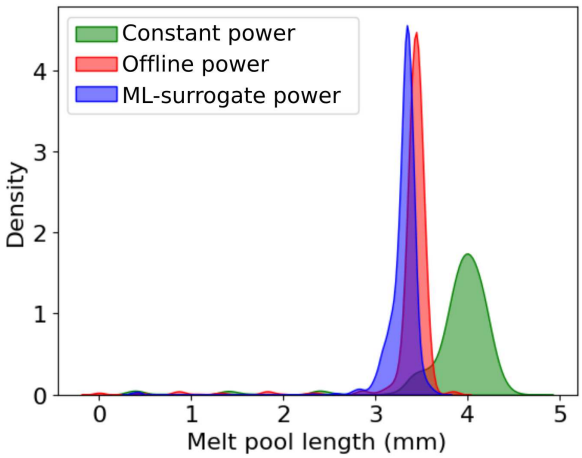
(b)



(c)



(d)



(e)

Figure 20: Infill-partitioned cubic deposition: (a) Time-series power profiles, (b) simulation results of the penetration depth, (c) density plot illustrating the distribution of the penetration depth, (d) simulation results of the melt pool length, (e) density plot illustrating the distribution of the melt pool length.

Table 6: Melt pool characteristics based on different power strategies.

Criteria	Constant power/ %	Offline designed power/ %	ML-surrogate designed power/ %
Penetration depth (0.38 mm - 0.42 mm)	1.09	96.43	87.68
Melt pool length (3.18 mm - 3.52 mm)	1.69	84.64	87.54

The SHapley Additive exPlanations (SHAP) [48] framework applies principles from the coalition game theory to calculate Shapley values, to interpret the predictions of ML models. This model-agnostic interpretability technique has been applied to the predictions of the developed ML model to characterize the importance of each input feature on the infill-partitioned cubic deposition test case. Shapley values were determined using the *KernelSHAP* method [48], which assigns an importance score (SHAP value) to each feature, quantifying their contributions to the predictions of the ML model [49, 50]. Figure 21 provides insights into feature importance and their impact on the predictions of the ML by displaying SHAP values across all samples. Input features are ranked by importance from top to bottom based on their absolute SHAP values, with dots representing the SHAP value of each input feature for individual predictions. The horizontal spread shows the range of impact, while the color gradient indicates feature value, with red representing higher values, clarifying if such a feature has the tendency to increase or decrease the output of the model. In this context, positive SHAP values indicate that an input feature contributes to an increase in the predicted laser power supply, whereas negative SHAP values indicate that it contributes to a decrease in the predicted laser power supply.

The next region temperature representing the substrate temperature significantly influences the output of the ML model. The latter has a negative impact on the ML predictions, suggesting the need for power reduction throughout the deposition process to minimize heat buildup. The melt pool, pulse and maximum temperatures are essential for the ML predictions and positively related to the power supply, indicating that to maintain thermal stability, the power supply needs to increase periodically. The melt pool volume and penetration are positively related to the predicted power, implying that to maintain the corresponding morphological characteristics constant throughout the deposition, a systematic increase in power is needed. The melt pool volume has a greater impact on the power, as more energy is needed to keep the uniformity of the melt pool volume as compared to the penetration depth. On the other hand, the melt pool length is negatively related to the power supply, suggesting that a decrease of power is needed to maintain the melt pool length stability. This may be due to better heat distribution along the melt pool length, hence reducing the need for an increase in power. The next region penetration, as detailed in Section 2.3.1, functions as a safeguard to prevent hallucinations during the predictions hence, it has no influence on the output of the model as observed in the SHAP plot.

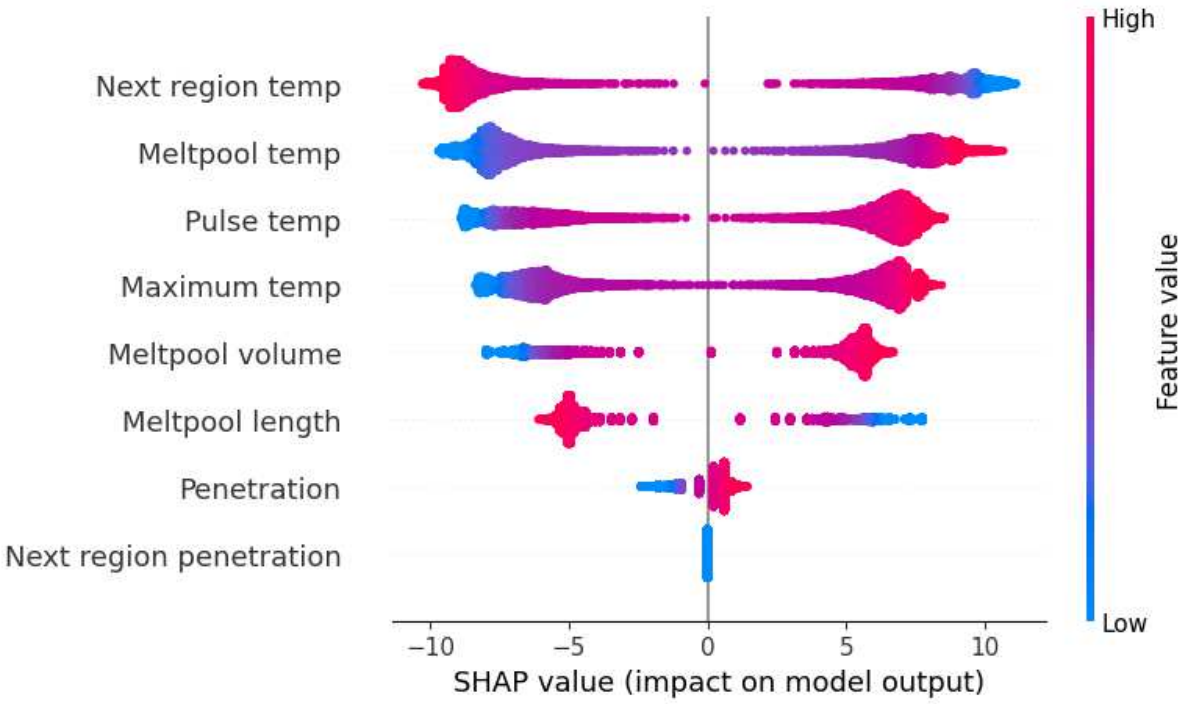


Figure 21: SHAP plot summary demonstrating the importance of each input feature for the ML predictions based on the infill-partitioned cubic deposition test case.

4 Conclusions

This work presents a Machine Learning (ML) based surrogate control strategy for the Laser-based Direct Energy Deposition (DED-LB) process, aimed at controlling the melt pool morphology throughout the deposition process. By employing a ML model coupled with a Finite Element (FE) solver, the proposed method enables the run-time determination of the optimized laser power profile necessary for achieving the desired melt pool stability. Numerical techniques facilitated the quantification of the melt pool depth, a feature not achievable through experimental methods during a material deposition process. The architecture of the ML model was determined through a hyperparameter tuning and trained using synthetic data generated from an offline iterative optimization process. Input features, such as melt pool geometric signatures and thermal profiles, were selected based on Spearman's correlation coefficients derived from the synthetic dataset. Key contributions and findings include:

(1) The developed ML-based surrogate control framework enables the derivation of a variable laser power profile that ensures constant melt pool penetration depth in a single iteration, eliminating the need for iterative optimization via simulations or experimental trial and error.

(2) With the proposed method, the power profile is autonomously determined by the ML-based surrogate control system, achieving results at a pace 3 times faster than the offline optimization approach. This significantly enhances prototyping capabilities, which are vital in Additive Manufacturing (AM) for enabling rapid design validation, cost reduction, and the incorporation of greater design complexity.

(3) Another novel aspect of this work is the prediction of the optimized power profile by the ML-based surrogate control framework for structural parts not included in the training dataset of the ML model. The synthetic dataset, consisting of High-Fidelity (HF) simulation results for single-hatch solid thin walls deposited in a unidirectional and bidirectional manner, provided a robust pool of data for the training of the ML model. This enables the latter to accurately generalize and predict the optimized power profiles for different scanning sequences. The ML model generated a power profile closely matching that of the offline optimization process for a hollow and an infill-partitioned

cubic deposition scanning sequence. Notably, an average of 97.47 % of the melt pool penetration depth in the offline approach and 89.73 % in the ML-based surrogate control approach fall within 0.38 mm to 0.42 mm, demonstrating the effectiveness of the ML-based surrogate control framework.

(4) As a conclusion of the test cases, it can be shown that the ML-based surrogate control system effectively generates the necessary power reduction to minimize heat accumulation during the material deposition process, thereby maintaining a consistent melt pool penetration depth. Additionally, the surrogate-generated power profile closely aligns with the offline counterpart, and the melt pool characteristics, including the penetration depth and length, consistently match the benchmark established by the offline optimization throughout the three numerical cases presented.

(5) A SHAP plot was developed to analyze the impact of input features on the predictions of the ML model. The findings demonstrate that the thermal characteristics of the deposition process are paramount in influencing the predictability of the power supply, outweighing the impact of melt pool geometrical features. Monitoring the substrate temperature and melt pool length, along with the penetration depth of the laser, was identified as critical for accurate power predictions. This indicates potential extra parameters for in-situ monitoring strategies during experimental campaigns to better qualify the laser power supply.

In future work, efforts will be directed towards enhancing the generalization and sensitivity capabilities of the ML-based surrogate model, for instance, by training it with additional synthetic data generated from a broader range of scanning sequences. In addition, Recurrent Neural Networks (RNNs) offer improvements for time-series data monitoring over traditional regression networks. While regression networks model static input-output relationships, RNNs capture temporal dependencies through their memory of past inputs, enhancing applications like predictive maintenance and process monitoring. Therefore, the potential of using a RNN model as a surrogate controller for the DED-LB process will be investigated with the aim of enhancing processing parameter identification, thereby enabling a more responsive control system.

Declarations

Acknowledgements

This project has received funding from the European Union's Horizon 2020 research and innovation programme under the Marie Skłodowska-Curie grant agreement Nº 101034328.

Carlos A. Moreira gratefully acknowledges the Juan de la Cierva grant JDC2022-049588-I, funded by MCIN/AEI/10.13039/501100011033 and by the European Union NextGenerationEU/PRTR.

The authors gratefully acknowledge the Beijing Institute of Aeronautical Materials (BIAM) for their valuable contributions and support in this research. The financial support of AECC BIAM through the project "Research and Development on Hybrid Forming Technology based on Titanium Alloy Investment Casting and Additive Manufacturing. Numerical Simulation and Experimental Characterization" is also acknowledged.

This work has been supported by the Ministry of Science, Innovation and Universities (MCIU) through the DIGITAM project (Desarrollo de un Gemelo Digital para Monitorización y el Control Activo del Proceso de Fabricación Aditiva DED), ref. num. CPP2023-010440.

Declaration of competing interest

The authors declare that they have no known competing financial interests or personal relationships that could have appeared to influence the work reported in this paper.

Data availability

Data will be made available on request.

Preprint Sharing

A preliminary version of this manuscript was deposited as a preprint on Research Square (DOI: `https://doi.org/10.21203/rs.3.rs-8641262/v1`).

References

[1] L. Chen, X. Yao, P. Xu, S. K. Moon, and G. Bi, "Rapid surface defect identification for additive manufacturing with in-situ point cloud processing and machine learning," *Virtual and Physical Prototyping*, vol. 16, no. 1, pp. 50–67, 2021.

[2] Z. Wang, T. A. Palmer, and A. M. Beese, "Effect of processing parameters on microstructure and tensile properties of austenitic stainless steel 304l made by directed energy deposition additive manufacturing," *Acta Materialia*, vol. 110, pp. 226–235, 2016.

[3] N. Shamsaei, A. Yadollahi, L. Bian, and S. M. Thompson, "An overview of direct laser deposition for additive manufacturing; part ii: Mechanical behavior, process parameter optimization and control," *Additive manufacturing*, vol. 8, pp. 12–35, 2015.

[4] S. Liao, S. Webster, D. Huang, R. Council, K. Ehmann, and J. Cao, "Simulation-guided variable laser power design for melt pool depth control in directed energy deposition," *Additive Manufacturing*, vol. 56, p. 102912, 2022.

[5] H. Rezaeifar and M. Elbestawi, "On-line melt pool temperature control in l-pbf additive manufacturing," *The International Journal of Advanced Manufacturing Technology*, vol. 112, no. 9, pp. 2789–2804, 2021.

[6] Z. Hu and W. Yuan, "Finite element analysis for residual stress of tb18 billet produced by laser directed energy deposition," *Materials Research Express*, vol. 10, no. 3, p. 036511, 2023.

[7] B. Kavas, E. C. Balta, M. R. Tucker, R. Krishnadas, A. Rupenyan, J. Lygeros, and M. Bambach, "In-situ controller autotuning by bayesian optimization for closed-loop feedback control of laser powder bed fusion process," *Additive Manufacturing*, vol. 99, p. 104641, 2025.

[8] N. Menon, S. Mondal, and A. Basak, "Multi-fidelity surrogate-based process mapping with uncertainty quantification in laser directed energy deposition," *Materials*, vol. 15, no. 8, p. 2902, 2022.

[9] F. Hermann, A. Michalowski, T. Brünnette, P. Reimann, S. Vogt, and T. Graf, "Data-driven prediction and uncertainty quantification of process parameters for directed energy deposition," *Materials*, vol. 16, no. 23, p. 7308, 2023.

[10] W. Liu, H. Liu, W. Li, B. Liu, Z. Ma, J. Song, T. Wang, Z. Lyu, G. Hu, H. Fan *et al.*, "A physical simulation-machine learning model for optimal process schemes in laser-based directed energy deposition process," *Optics & Laser Technology*, vol. 177, p. 111096, 2024.

[11] T. Wuest, D. Weimer, C. Irgens, and K.-D. Thoben, "Machine learning in manufacturing: advantages, challenges, and applications," *Production & Manufacturing Research*, vol. 4, no. 1, pp. 23–45, 2016.

[12] W. L. Ng, G. L. Goh, G. D. Goh, J. S. J. Ten, and W. Y. Yeong, "Progress and opportunities for machine learning in materials and processes of additive manufacturing," *Advanced Materials*, vol. 36, no. 34, p. 2310006, 2024.

[13] L. Meng, B. McWilliams, W. Jarosinski, H.-Y. Park, Y.-G. Jung, J. Lee, and J. Zhang, "Machine learning in additive manufacturing: a review," *Jom*, vol. 72, pp. 2363–2377, 2020.

[14] G. D. Goh, S. L. Sing, and W. Y. Yeong, "A review on machine learning in 3d printing: applications, potential, and challenges," *Artificial Intelligence Review*, vol. 54, no. 1, pp. 63–94, 2021.

[15] M. Parsazadeh, S. Sharma, and N. Dahotre, "Towards the next generation of machine learning models in additive manufacturing: A review of process dependent material evolution," *Progress in Materials Science*, vol. 135, p. 101102, 2023.

[16] C. Snyers, J. Ertveldt, J. Sanchez-Medina, Z. Jardon, and J. Helsen, "Prediction of build geometry for ded using supervised learning methods on simulated process monitoring data," *Journal of Laser Applications*, vol. 33, no. 4, 2021.

[17] S. Fetni, Q. D. T. Pham, V. X. Tran, L. Duchêne, H. S. Tran, and A. M. Habraken, "Thermal field prediction in ded manufacturing process using artificial neural network," *ESAFORM 2021 — 24th International Conference on Material Forming*, 2021.

[18] C. Wang, X. P. Tan, S. B. Tor, and C. Lim, "Machine learning in additive manufacturing: State-of-the-art and perspectives," *Additive Manufacturing*, vol. 36, p. 101538, 2020.

[19] S. Dharmadhikari, N. Menon, and A. Basak, "A reinforcement learning approach for process parameter optimization in additive manufacturing," *Additive Manufacturing*, vol. 71, p. 103556, 2023.

[20] F. Ogoke and A. B. Farimani, "Thermal control of laser powder bed fusion using deep reinforcement learning," *Additive Manufacturing*, vol. 46, p. 102033, 2021.

[21] O. Kwon, H. G. Kim, M. J. Ham, W. Kim, G.-H. Kim, J.-H. Cho, N. I. Kim, and K. Kim, "A deep neural network for classification of melt-pool images in metal additive manufacturing," *Journal of Intelligent Manufacturing*, vol. 31, pp. 375–386, 2020.

[22] S. Ho, W. Zhang, W. Young, M. Buchholz, S. Al Jufout, K. Dajani, L. Bian, and M. Mozumdar, "Dlam: Deep learning based real-time porosity prediction for additive manufacturing using thermal images of the melt pool," *IEEE Access*, vol. 9, pp. 115 100–115 114, 2021.

[23] O. Kwon, H. G. Kim, W. Kim, G.-H. Kim, and K. Kim, "A convolutional neural network for prediction of laser power using melt-pool images in laser powder bed fusion," *IEEE Access*, vol. 8, pp. 23 255–23 263, 2020.

[24] R. Ghanavati and H. Naffakh-Moosavy, "Additive manufacturing of functionally graded metallic materials: A review of experimental and numerical studies," *Journal of Materials Research and Technology*, vol. 13, pp. 1628–1664, 2021.

[25] J. Ye, A. Bab-Hadiashar, R. Hoseinnezhad, N. Alam, A. Vargas-Uscategui, M. Patel, and I. Cole, "Predictions of in-situ melt pool geometric signatures via machine learning techniques for laser metal deposition," *International Journal of Computer Integrated Manufacturing*, vol. 36, no. 9, pp. 1345–1361, 2023.

[26] J. Dilip, S. Zhang, C. Teng, K. Zeng, C. Robinson, D. Pal, and B. Stucker, "Influence of processing parameters on the evolution of melt pool, porosity, and microstructures in ti-6al-4v alloy parts fabricated by selective laser melting, prog. addit. manuf. 2 (2017) 157–167," 2017.

[27] M. Khanzadeh, S. Chowdhury, M. A. Tschopp, H. R. Doude, M. Marufuzzaman, and L. Bian, "In-situ monitoring of melt pool images for porosity prediction in directed energy deposition processes," *Iise Transactions*, vol. 51, no. 5, pp. 437–455, 2019.

[28] C. A. Moreira, M. Chiumenti, J. Baiges, H. Venghaus, X. Lu, X. Liao, T. Herzog, A. E. Medvedev, A. Molotnikov, M. Cervera *et al.*, "Simulation-based qualification of repair and remanufacturing operations through ded technology of ti6al4v parts," *Progress in Additive Manufacturing*, pp. 1–38, 2026.

[29] J. Baiges, M. Chiumenti, C. A. Moreira, M. Cervera, and R. Codina, "An adaptive finite element strategy for the numerical simulation of additive manufacturing processes," *Additive Manufacturing*, vol. 37, p. 101650, 2021.

[30] C. A. Moreira, M. A. Caicedo, M. Cervera, M. Chiumenti, and J. Baiges, "An accurate, adaptive and scalable parallel finite element framework for the part-scale thermo-mechanical analysis in metal additive manufacturing processes," *Computational Mechanics*, vol. 73, no. 5, pp. 983–1011, 2024.

[31] C. A. Moreira, M. Chiumenti, M. A. Caicedo, J. Baiges, and M. Cervera, "High-fidelity part-scale simulations in metal additive manufacturing using a computationally efficient and accurate approach," *Additive Manufacturing*, vol. 104, p. 104748, 2025.

[32] I. Setien, M. Chiumenti, M. San Sebastian, M. A. Caicedo, and C. A. Moreira, "Defining and optimising high-fidelity models for accurate inherent strain calculation in laser powder bed fusion," *Metals*, vol. 15, no. 2, p. 180, 2025.

[33] Sandia National Laboratories, "Dakota optimization software," 2023, accessed: February, 2025. [Online]. Available: https://dakota.sandia.gov/

[34] I. Jeon, L. Yang, K. Ryu, and H. Sohn, "Online melt pool depth estimation during directed energy deposition using coaxial infrared camera, laser line scanner, and artificial neural network," *Additive Manufacturing*, vol. 47, p. 102295, 2021. [Online]. Available: https://www.sciencedirect.com/science/article/pii/S2214860421004553

[35] C. A. Moreira, M. A. Caicedo, M. Cervera, M. Chiumenti, and J. Baiges, "A multi-criteria h-adaptive finite-element framework for industrial part-scale thermal analysis in additive manufacturing processes," *Engineering with Computers*, vol. 38, no. 6, pp. 4791–4813, 2022.

[36] C. Spearman, "The proof and measurement of association between two things," in *Studies in individual differences: The search for intelligence*, J. J. Jenkins and D. G. Paterson, Eds. Appleton-Century-Crofts, 1961, pp. 45–58.

[37] J. Hauke and T. Kossowski, "Comparison of values of pearson's and spearman's correlation coefficients on the same sets of data," *Quaestiones geographicae*, vol. 30, no. 2, pp. 87–93, 2011.

[38] P. I. Frazier, "Bayesian optimization," in *Recent advances in optimization and modeling of contemporary problems*. Informs, 2018, pp. 255–278.

[39] F. Chollet, "Keras," https://keras.io, 2015.

[40] A. Krizhevsky, I. Sutskever, and G. E. Hinton, "Imagenet classification with deep convolutional neural networks," *Advances in neural information processing systems*, vol. 25, 2012.

[41] B. Xu, N. Wang, T. Chen, and M. Li, "Empirical evaluation of rectified activations in convolutional network," *arXiv preprint arXiv:1505.00853*, 2015.

[42] D. P. Kingma and J. Ba, "Adam: A method for stochastic optimization," *arXiv preprint arXiv:1412.6980*, 2014.

[43] N. Fernandez, "Forpy: Fortran-python interoperability library," GitHub repository, 2023, accessed: 2025-04-28. [Online]. Available: https://github.com/ylikx/forpy

[44] I. Jeon, L. Yang, K. Ryu, and H. Sohn, "Online melt pool depth estimation during directed energy deposition using coaxial infrared camera, laser line scanner, and artificial neural network," *Additive Manufacturing*, vol. 47, p. 102295, 2021.

[45] T. DebRoy, H. L. Wei, J. S. Zuback, T. Mukherjee, J. W. Elmer, J. O. Milewski, A. M. Beese, A. d. Wilson-Heid, A. De, and W. Zhang, "Additive manufacturing of metallic components–process, structure and properties," *Progress in materials science*, vol. 92, pp. 112–224, 2018.

[46] R. Mahamood and E. Akinlabi, "Effect of powder flow rate on surface finish in laser additive manufacturing process," in *IOP Conference Series: Materials Science and Engineering*, vol. 391, no. 1. IOP Publishing, 2018, p. 012005.

[47] A. Saboori, D. Gallo, S. Biamino, P. Fino, and M. Lombardi, "An overview of additive manufacturing of titanium components by directed energy deposition: microstructure and mechanical properties," *Applied Sciences*, vol. 7, no. 9, p. 883, 2017.

[48] S. M. Lundberg and S.-I. Lee, "A unified approach to interpreting model predictions," *Advances in neural information processing systems*, vol. 30, 2017.

[49] I. Ekanayake, D. Meddage, and U. Rathnayake, "A novel approach to explain the black-box nature of machine learning in compressive strength predictions of concrete using shapley additive explanations (shap)," *Case Studies in Construction Materials*, vol. 16, p. e01059, 2022.

[50] L. Antwarg, R. M. Miller, B. Shapira, and L. Rokach, "Explaining anomalies detected by autoencoders using shapley additive explanations," *Expert systems with applications*, vol. 186, p. 115736, 2021.